Bioorganic Chemistry 179 (2026) 110016

Contents lists available at ScienceDirect

Bioorganic Chemistry

journal homepage: www.elsevier.com/locate/bioorg

Structure-selective binding and bioactivity of chlorine-substituted cyanine dyes with DNA, RNA, and lipid membranes

Nina Vukadinović [a], Ivo Crnolatac [a], Atanas Kurutos [b,c,**], Petra Jadrijević-Mladar [d], Lidija-Marija Tumir [a], Anamaria Brozovic [d], Ana Tomašić Paić [a], Lucija Horvat [d], Marijana Radić Stojković [a,*]

[a] Division of Organic Chemistry and Biochemistry, Ruđer Bošković Institute, Bijenička cesta 54, 10000 Zagreb, Croatia
[b] Institute of Organic Chemistry with Centre of Phytochemistry, Bulgarian Academy of Sciences, Acad. G. Bonchev str., bl. 9, Sofia 1113, Bulgaria
[c] University of Chemical Technology and Metallurgy, 8 St. Kliment Ohridski Blvd, 1756 Sofia, Bulgaria
[d] Division of Molecular Biology, Ruđer Bošković Institute, Bijenička cesta 54, 10000 Zagreb, Croatia

ARTICLE INFO

Keywords:
Cyanines
DNA/RNA
Quadruplex
Liposome
Antitumour
Antibacterial

ABSTRACT

A comprehensive physicochemical and biological evaluation of three cyanine dyes revealed clear structure-dependent differences in their interactions with nucleic acids, lipid membranes, and cells. Two monomethine derivatives interacted moderately and non-specifically with ds-DNA/RNA, producing weak thermal stabilisation and no induced CD signals, consistent with external binding. The monomethine benzoxazole-containing dye showed strong antibacterial activity against *Staphylococcus aureus*, comparable to ampicillin, and promising anticancer activity with selectivity over normal fibroblasts. In contrast to monomethine derivatives, the trimethine dye displayed highly selective nucleic acid recognition, including a dual fluorimetric response toward AU-RNA and distinct induced CD signatures for all examined polynucleotides. It's marked ICD differences between monomeric and aggregated species—especially the opposite helical arrangements detected for GC- and IC-DNA—demonstrate a remarkably high level of structural sensitivity for dyes of this class. The trimethine dye further discriminated Tel22 G-quadruplex topologies in K^+ and Na^+ solutions through ICD signature. Altogether, it emerges as a highly structure-responsive probe capable of differentiating nucleic acid conformations via both fluorescence and ICD readouts, highlighting the broader potential of chlorinated cyanine dyes for nucleic acid sensing and biomedical applications.

1. Introduction

Selective recognition of nucleic acid structures by small molecules is a rapidly advancing field with considerable significance in diagnostics and therapeutic development [1]. DNA and RNA exist in a range of structural forms—single-stranded, double-stranded, triplexes, and quadruplexes—each presenting unique binding opportunities for synthetic ligands [2]. Noncovalent interactions dominate this molecular recognition, mostly involving intercalation between base pairs, groove binding, and electrostatic interactions between the negatively charged phosphate backbone and cationic molecules.

Cyanine dyes have emerged as a versatile class of fluorescent probes due to their characteristic “light-up” fluorescence behaviour upon nucleic acid binding, contrasting their low emission in solution [3–6]. Detailed quantum mechanical and spectroscopic analyses of thiazole orange (TO), a prototypical cyanine dye, have shown that even slight modifications in its structure or binding environment can dramatically influence its photophysical properties and nucleic acid affinity [7].

Recently, we reported on dicationic monomethine cyanines—both halogenated and non-halogenated—that can drive the formation of RNA/DNA triplex helices, particularly in rA/dA-rich sequences [8]. The chlorinated derivatives in this series were especially effective, stabilising triplex structures and promoting H-aggregate formation in the presence of rA segments in single-stranded, double-stranded, or triple-stranded nucleic acid conformations. A further study of neutral and mono-cationic asymmetric monomethine cyanine dyes bearing a

* Corresponding author.
** Corresponding author at: Institute of Organic Chemistry with Centre of Phytochemistry, Bulgarian Academy of Sciences, Acad. G. Bonchev str., bl. 9, Sofia 1113, Bulgaria.
E-mail addresses: akouroutos@gmail.com (A. Kurutos), mradic@irb.hr (M. Radić Stojković).

https://doi.org/10.1016/j.bioorg.2026.110016
Received 24 February 2026; Received in revised form 13 May 2026; Accepted 20 May 2026
Available online 22 May 2026
0045-2068/© 2026 The Authors. Published by Elsevier Inc. This is an open access article under the CC BY license (http://creativecommons.org/licenses/by/4.0/).

benzoselenazolyl group revealed that the methyl- and chlorine-substituted analogues bind selectively to G-quadruplexes. At the same time, the thioethyl derivative could differentiate between duplex DNA/RNA and G-quadruplex structures through distinct CD signatures [9,10]. Confocal microscopy confirmed subcellular localization, with sulfopropyl and thioethyl derivatives targeting mitochondria and the methyl-substituted dye accumulating in the nucleolus.

Due to interactions with nucleic acids, monomethine cyanine dyes are widely employed in molecular biology for detecting and quantifying DNA or RNA in complex samples, including DNA staining, real-time PCR, and gel electrophoresis [11,12]. In contrast, JC-1, a cationic carbocyanine dye, is primarily used to monitor mitochondrial membrane potential (Δψm) in live cells. At high membrane potential, JC-1 forms red-fluorescent aggregates, whereas in depolarized or apoptotic cells, it exists as green-fluorescent monomer, enabling a ratiometric assessment of mitochondrial health [13–15]. This unique property makes JC-1 a key tool in apoptosis research, toxicology, and mitochondrial physiology studies [16]. Further, fluorescent dyes embedded in liposomes are a well-established method for monitoring drug–membrane interactions and thermally induced changes in membranes [17,18]. Based on our literature search, information on JC-1 binding to DNA and RNA, as well as its interactions with liposomes, remains limited. Therefore, a key objective of this study is to explore and gain a deeper understanding of these interactions and their biological effect.

Here, we investigated three chlorinated cyanine derivatives: two asymmetric momomethine dyes with benzoxazole and benzothiazole moieties (**AK-Z1**, **AK-Z2**), and a trimethine JC-1 dye with benzimidazole units (**AK-Z4**). The goals of the investigation included 1) the binding study of **AK-Z1**, **AK-Z2** and **AK-Z4** with DNA and RNA, 2) their interactions with liposomes, and 3) study of their effect on cell proliferation, bacterial inhibition, and determination of their intracellular localization. We employed UV/Vis absorption and fluorescence spectroscopy, thermal melting studies, and circular dichroism (CD) spectroscopy to evaluate the binding affinity, spectral response, and binding mode of the cyanine dyes with DNA. Differential Scanning Calorimetry (DSC) and fluorimetry were utilized for drug–membrane interaction study. To assess their biological potential, we conducted 3-(4,5-dimethylthiazol-2-yl)-2,5-diphenyltetrazolium bromide (MTT) and AlamarBlue cytotoxicity assays and performed confocal fluorescence microscopy to investigate cellular uptake and localization. Furthermore, the antibacterial effect was evaluated using the broth microdilution method.

2. Results and discussion

2.1. Synthesis

Intermediates **1–4**, as well as the target cyanines were prepared according to the reported protocols found in the literature [19–23]. Due to the hygroscopic nature and the stability of intermediates, they were used directly in the synthesis of the target fluorophores without additional purification.

For the **AK-Z4** compound, our method differs by using the iodide salt, triethyl orthoformate, and DIPEA, and uniquely employing 1,2-dichlorobenzene as the reaction solvent, a combination not previously reported for JC-1 synthesis [24–26].

3-(3-(acetylthio)propyl)-2-((5,6-dichloro-1,3-diethyl-1,3-dihydro-2H-benzo[d]imidazol-2-ylidene)methyl)benzo[d]oxazol-3-ium iodide (**AK-Z1**):

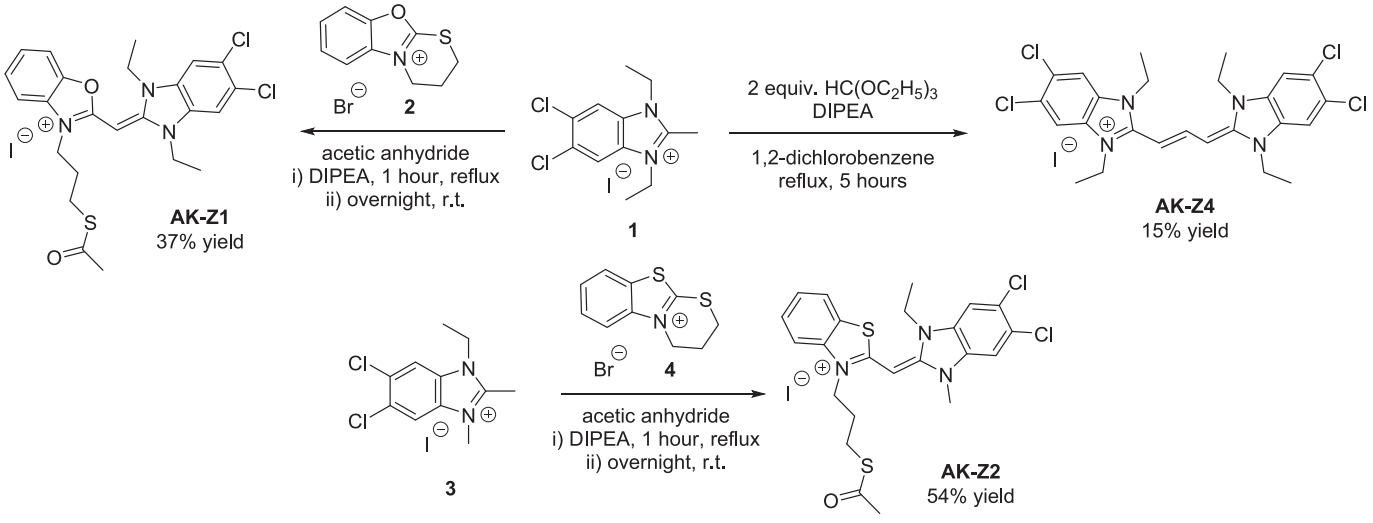
Equimolar amounts of **1** (1.0 equiv., 516 mg, 2.0 mmol) and intermediate **2** (1.0 equiv., 508 mg, 2.0 mmol) were suspended in 10 mL acetic anhydride. A slight excess of *N,N*-Diisopropylethylamine - DIPEA (1.1 equiv., 0.38 mL, 2.2 mmol) was added, and the resulting mixture was refluxed for 1 h. The flask content was left stirring overnight at room temperature (Scheme 1). The target product was precipitated in 365 mg (37% yield) as a yellow powder (m.p. 208–209 °C) by the addition of diethyl ether and filtered under reduced pressure.

3-(3-(acetylthio)propyl)-2-((5,6-dichloro-1-ethyl-3-methyl-1,3-dihydro-2H-benzo[d]imidazol-2-ylidene)methyl)benzo[d]thiazol-3-ium iodide (**AK-Z2**):

Equimolar amounts of **3** (1.0 equivalent, 516 mg, 2.0 mmol) and intermediate **4** (1 equiv., 540 mg, 2.0 mmol) were suspended in 10 mL of acetic anhydride. A slight excess of *N,N*-Diisopropylethylamine – DIPEA (1.1 equiv., 0.38 mL, 2.2 mmol) was added, and the resulting mixture was refluxed for 1 h. The flask content was left stirring overnight at room temperature (Scheme 1). The target product was precipitated in 550 mg (54% yield) as deep-orange flakes (m.p. 245–246 °C) with metallic shine by the addition of diethyl ether and filtered under reduced pressure.

5,6-dichloro-2-(3-(5,6-dichloro-1,3-diethyl-1,3-dihydro-2H-benzo[d]imidazol-2-ylidene)prop-1-en-1-yl)-1,3-diethyl-1H-benzo[d]imidazol-3-ium iodide (**AK-Z4**):

Intermediate **1** (1.0 equiv., 516 mg, 2.0 mmol), triethylorthoformate (2.0 equiv., 0.66 mL, 4.0 mmol), and *N,N*-Diisopropylethylamine - DIPEA (2.0 equiv., 0.35 mL, 2.0 mmol) were mixed with 10 mL 1,2-dichlorobenzene and refluxed for 5 h. Upon cooling down to room temperature, the resulting precipitate was filtered under reduced pressure and washed with diethyl ether (3 × 50 mL), affording 138 mg (15% yield) of the target **AK-Z4** dye as green powder with metallic shine.



Scheme 1. Synthetic approach to the preparation of the target fluorophores.

Analytical samples for all three dyes were obtained after repeated recrystallizations from ethanol.

We assume that the enhanced yield of the benzothiazolium derivative (**AK-Z2**, 54%) compared to the isolated yield of the benzoxazolium dye (**AK-Z1**, 37%) may be attributed to the superior stability of the quaternary ammonium salt **4** in comparison to intermediate **2** employed for the synthesis of the **AK-Z1** dye. Our prior experience in that field indicates that under the same reaction conditions, oxygen-containing quaternary salts with a structure analogous to intermediate **2**, typically exhibit reduced stability compared to benzothiazolium building blocks (e.g., intermediate **4**) when utilized as a precursor for the cyanine dye synthesis. The suboptimal yield of the symmetrical **AK-Z4** (15%) chromophore may be ascribed to the instability of either the target dye or the intermediate during reflux in a relatively high boiling point solvent such as 1,2-dichlorobenzene. Many quaternary ammonium compounds typically suffer from decomposition when subjected to temperatures exceeding 130 °C for prolonged times. Last but not least, the reduced yield may also be ascribed to the partial solubility of the target product in 1,2-dichlorobenzene, which additionally caused loss during the isolation of the crude dye.

2.2. Spectroscopic characterization of AK-Z1, AK-Z2 and AK-Z4 in the aqueous media

All compounds, **AK-Z1**, **AK-Z2** and **AK-Z4** were dissolved ($c = 5 \times 10^{-3}$ mol dm^{-3}) in dimethyl sulfoxide (DMSO) and diluted with buffer (sodium cacodylate buffer, $I = 0.05$ mol dm^{-3}, pH = 7.0) for measurements. The volume ratio of DMSO was less than 1% in all measurements. The absorbances of buffered solutions of studied compounds (Fig. 1) are proportional to their concentrations up to $c = 4 \times 10^{-6}$ mol dm^{-3} (Figs. S1-S4 in the Supporting information (SI)). Absorption maxima with corresponding molar extinction coefficients (ε) and quantum yields (QY) of studied compounds and complexes with nucleic acid sequences are given in the SI (Table S1).

Fluorescence emissions of the studied compounds (Fig. 1) were linearly dependent on their concentrations up to $c = 2 \times 10^{-6}$ mol dm^{-3} (Figs. S5-S7 in the Supporting information (SI)). Excitation spectra recorded at emission maxima are in good agreement with UV/Vis spectra.

JC-1 (denoted here as **AK-Z4**) exists in aqueous solution predominantly as a monomer, exhibiting excitation and emission peaks in the green spectral range, and, under favourable conditions, as J-aggregates [13,27]. Unlike the monomer, the J-aggregates display identical excitation and emission maxima, with essentially no Stokes shift. The formation of J-aggregates is highly dependent on environmental factors, such as dye concentration, pH, ionic strength, and temperature.

In this study, experiments were performed in buffer at pH 7.0 and ionic strength ≥0.05 M to mimic physiological conditions. Under these conditions, monomeric and aggregated forms of **AK-Z4** coexist in solution.

All experiments were carried out at room temperature, except for thermal melting assays. To assess thermal stability, absorption spectra of the compounds were recorded during heating and subsequent cooling to room temperature. For **AK-Z1** and **AK-Z2**, changes in absorption maxima were negligible upon heating to 95 °C, and spectral profiles were fully restored after cooling to 25 °C.

In contrast, **AK-Z4** showed significant spectral changes upon heating. The monomer absorption peak increased markedly (by 183%), while the aggregate peak decreased substantially (by 72%), indicating thermally induced dissociation of aggregates into monomer species (Fig. S4 in the SI). After cooling to 25 °C, both absorption maxima nearly returned to their initial values, demonstrating reversible behaviour.

The time-resolved fluorescence measurements of the dyes in the 100 mM phosphate buffer pH 7.2 were also performed at room (20 °C) and elevated (50 °C) temperatures. At both temperatures, **AK-Z1** and **AK-Z2** were predominantly present as a single relatively short-lived fluorescent species ($\tau < 0.3$ ns). In contrast, **AK-Z4** showed more complex behaviour, with at least three distinct emissive species detected. In this case, longer-lived fluorescence species (3 ns $< \tau <$ 7 ns) were the dominant populations (Table S3 in SI).

2.3. Interactions of AK-Z1, AK-Z2 and AK-Z4 with DNA and RNA

The interactions of **AK-Z** compounds were investigated using natural

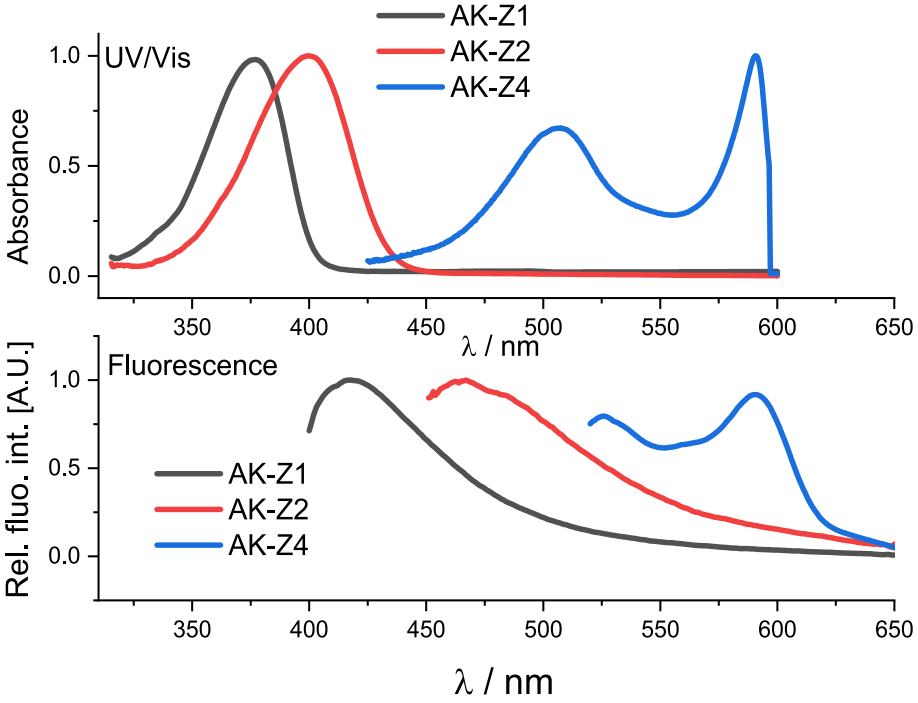


Fig. 1. Normalized UV/Vis and fluorescence spectra of **AK-Z1** (λ_{exc} = 377 nm, λ_{em} = 421 nm), **AKZ2** (λ_{exc} = 401 nm, λ_{em} = 463 nm) and **AKZ4** (λ_{exc} = 501, 591 nm, λ_{em} = 530, 591 nm) in aqueous solution (sodium cacodylate buffer, $I = 0.05$ mol dm^{-3}, pH = 7.0).

and synthetic polynucleotides differing in base composition and secondary structure. Natural calf-thymus (ct) DNA (58% AT, 42% GC) and synthetic ds-polynucleotides were selected to evaluate the influence of structural features such as groove size and shape on binding [28].

Representative B-helical structures included ctDNA, poly(dAdT)·poly(dAdT) (AT-DNA), and poly(dGdC)·poly(dGdC) (GC-DNA), the latter possessing a minor groove sterically hindered by guanine amino groups [29]. Poly(rA)·poly(rU) (AU-RNA), used as a representative A-helical structure, is characterized by a wide, shallow minor groove and a deep, narrow major groove [30].

2.3.1. Thermal melting studies

DNA melting temperature (T_m) is defined as the temperature at which half of the double helix dissociates into single strands due to disruption of hydrogen bonds between base pairs. It depends on several factors, including solution pH, salt concentration, DNA length, and GC content. Binding of small molecules can shift T_m: intercalators typically stabilise DNA through aromatic stacking, producing a positive ΔT_m (usually saturating at a ligand-to-nucleic acid ratio of $r = 0.2$), whereas minor-groove binders generally induce moderate to strong stabilisation. In contrast, ligand-induced destabilisation lowers T_m, resulting in a negative ΔT_m value [31]. The aggregation of ligands within DNA grooves can result in pronounced stabilisation, while nonspecific external binding has little effect.

The addition of the studied dyes to double-stranded (ds-) DNA produced moderate stabilisation of ctDNA, while the effects on AT-DNA were negligible (**AK-Z4**) or absent (**AK-Z1**, **AK-Z2**). These findings suggest that ctDNA stabilisation mainly arises from interactions with GC base pairs. Among the compounds, only **AK-Z2** showed slight stabilisation of AU-RNA (Table 1, Figs. S27-S29). Of all the compounds, **AK-Z4** showed the greatest stabilising effect on ctDNA. This behaviour is most likely related to its elongated planar π-conjugated system, which enables partial intercalation or groove binding of monomeric **AK-Z4** species, as well as binding of J-aggregates within or near DNA grooves. The negligible or absent stabilisation observed for AT-DNA and AU-RNA indicates predominantly external binding along the polynucleotide backbone.

2.3.2. Fluorimetric and UV/Vis titrations

The addition of ctDNA produced only minor or negligible changes in the fluorescence of **AK-Z1** and **AK-Z2**, preventing reliable determination of their binding affinities. Unlike **AK-Z4**, which showed a small red shift of up to 3 nm at 591 nm upon binding, the emission maxima of **AK-Z1** and **AK-Z2** remained unchanged in the presence of the studied polynucleotides. Titrations of **AK-Z4** with most polynucleotides resulted in fluorescence quenching. A sufficient number of collected data enabled a reliable calculation of binding constants (Figs. S8-S14). A distinct fluorimetric response was observed for AU-RNA. In this case, the addition of AU-RNA caused fluorescence quenching at the monomer emission peak (536 nm), accompanied by enhanced emission at the aggregate peak (591 nm) (Fig. 2). These changes, accompanied by a gradual shift away from the isosbestic region (567–573 nm), suggest the formation of two different **AK-Z4**-AU-RNA complexes.

Structurally, **AK-Z1** and **AK-Z2** contain a shorter bridge consisting of a single methine (–CH=) unit linking the benzo[*d*]oxazole (**AK-Z1**) or benzo[*d*]thiazole (**AK-Z2**) ring with the imidazole system. In contrast, **AK-Z4** features an extended polymethine bridge composed of three methine units connecting two benzimidazole rings. This larger π-conjugated system likely influences the electronic properties of **AK-Z4** and enhances its susceptibility to interactions with nucleic acids.

For most **AK-Z4** titrations, significant spectral changes were observed only in the aggregate emission peak, enabling reliable determination of the binding affinity (Table 2). The exception was AU-RNA, as changes in both monomer and aggregate emission peaks allowed separate analysis of the two binding processes. Binding constants were estimated from fluorimetric titration data using the Scatchard equation [32,33]. For the **AK-Z4**-AU-RNA complex, fluorescence quenching and enhancement data were analysed independently. **AK-Z4** exhibited comparably strong affinity toward both ds-DNA and ds-RNA, suggesting that variations in polynucleotide sequence or conformation do not substantially influence the binding affinity of the J-aggregate. For AU-RNA, where monomer binding could also be evaluated, the binding constant for the monomer species ($\log K_s = 6.4$) was approximately one order of magnitude lower than that determined for the J-aggregate complex (Table 2).

Since **AK-Z1** and **AK-Z2** have weak fluorescence, their interactions with polynucleotides could not be reliably assessed using fluorescence spectroscopy. Therefore, UV/Vis titrations were additionally performed (Figs. S15-S26). Interaction of the dyes with ds-DNA or RNA caused hypochromic effects (Table 3), accompanied either by no spectral shift (**AK-Z1** and **AK-Z2**) or by a pronounced red shift of 10–17 nm for **AK-Z4** at 501 nm.

The most significant hypochromic effect was observed for **AK-Z4** (Fig. 3). Analysis of the titration data with the Scatchard equation revealed similar binding affinities for the examined ds-DNA and ds-RNA, although **AK-Z4** showed a slightly higher affinity for AU-RNA. For **AK-Z4**, only the titration data at 501 nm (monomer absorption peak) were used for the calculation of stability constants, as the spectral changes at this wavelength were sufficient for reliable analysis.

2.3.3. Circular dichroism spectroscopy

To investigate conformational changes in polynucleotide secondary structure upon small-molecule binding, we used CD spectroscopy. Additional information on ligand–polynucleotide complexes and the binding mode can be gained from the induced CD (ICD) signals of achiral ligands, which reflect the mutual orientation of the ligand and the polynucleotide's chiral axis. When studied compounds absorb at $\lambda > 300$ nm, where polynucleotides do not absorb, ICD signals can be attributed to the ligands, offering reliable insight into their interactions with polynucleotides [34].

DNA can also serve as a chiral template that promotes dye aggregation via noncovalent binding and transfer chirality to the resulting supramolecular aggregates. Exciton-coupled bisignate ICD bands are considered strong evidence for the formation of ordered aggregates, such as H- and J-aggregates, along the polynucleotide backbone [35,36]. J-aggregates are characterized by narrow, red-shifted absorption bands relative to the monomer, whereas H-aggregates display blue-shifted absorption bands.

The addition of **AK-Z1** and **AK-Z2** to ds-DNA or ds-RNA caused negligible changes in the CD spectra of the polynucleotides (at 275 nm for ctDNA and GC-DNA, and at around 265 nm for AT-DNA and AU-RNA), confirming that the overall helicity of DNA/RNA remained preserved (Figs. S30-S31 in SI). No ICD signals were detected in the absorption region of these dyes, suggesting a non-uniform orientation of chromophore transition moments relative to the chiral axis of DNA/RNA structure and non-specific external binding [34].

In contrast, the addition of **AK-Z4** caused a slight decrease in the intensity of the CD bands of DNA and RNA polynucleotides, with the most pronounced effect observed for AU-RNA (Fig. 4 and Figs. S30-S31 in the SI). **AK-Z4** also produced strong ICD signals in its absorption

Table 1
The [a]ΔT_m values (°C) of studied ds-polynucleotides upon addition of ratio [b]r =0.2 of **AK-Z1**, **AK-Z2** and **AK-Z4** at pH 7.0 (sodium cacodylate buffer, $I = 0.05$ mol dm^{-3}).

[b]$r = 0.2$	AK-Z1	AK-Z2	AK-Z4
ctDNA	2.5	2.4	4.5
AT-DNA	0	0	0.7
AU-RNA	0	0.9	0

[a] Error in ΔT_m: ± 0.5 °C;
[b] r = [compound] / [polynucleotide].

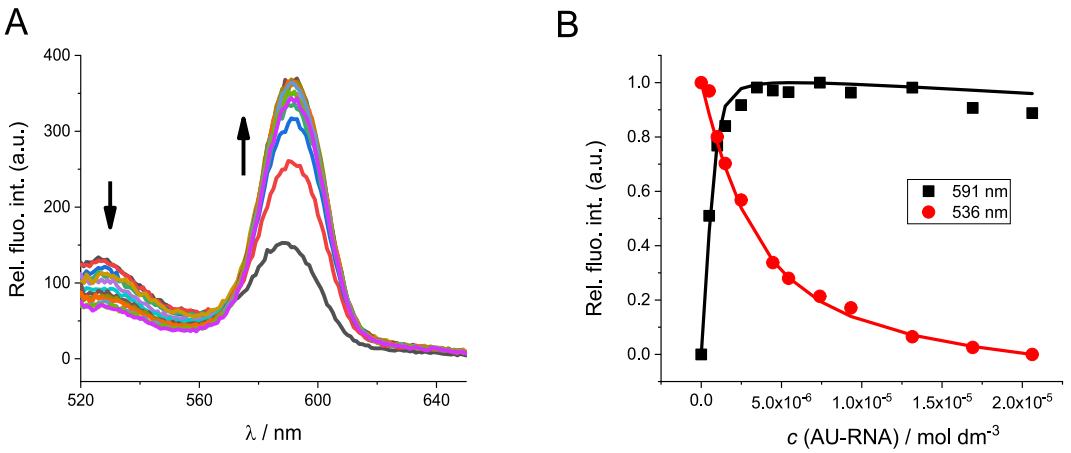


Fig. 2. **A**) Changes in fluorescence spectrum of **AKZ-4** ($c = 5.0 \times 10^{-7}$ mol dm^{-3}, $\lambda_{exc} = 501$ nm) upon titration with AU-RNA ($c = 5.0 \times 10^{-7}$–2.1×10^{-5} mol dm^{-3}); **B**) Dependence of normalized **AK-Z4** intensities and fitted values at $\lambda_{max} = 591$ (black) and 536 (red) nm on c (AU-RNA), at pH 7.0, sodium cacodylate buffer, $I = 0.05$ mol dm^{-3}. (For interpretation of the references to colour in this figure legend, the reader is referred to the web version of this article.)

Table 2
Binding constants (logK_s)[a,b] of complexes of **AK-Z4**[c] compounds with ds- polynucleotides at pH = 7.0 (sodium cacodylate buffer, $I = 0.05$ mol dm^{-3}) calculated from the fluorescence titrations.

ctDNA		AT-DNA		GC-DNA		AU-RNA	
logK_s	I/I$_0$[d]	logK_s	I/I$_0$[d]	logK_s	I/I$_0$[d]	logK_s	I/I$_0$[d]
7.5	0.6	7.1	0.4	6.9	0.5	7.4	2.4

[a,b] Processing of titration data using the Scatchard equation gave stability constants K_s; all K_s values were re-calculated with fixed value n([bound compound]/[polynucleotide phosphate]) = 0.5 for comparison reason; correlation coefficients were > 0.98 for all calculated K_s;

[c] A small fluorescence change and/or high divergences of absorbance intensities of **AK-Z1** and **AK-Z2** disabled the calculation of the stability constant.

[d] I_0 – starting fluorescence intensity of **AK-Z4** (aggregate peak); I – fluorescence intensity of **AK-Z4**/polynucleotide complex calculated by Scatchard equation.

Table 3
Binding constants (logK_s)[a,b] and spectroscopic changes[d] calculated from the UV/Vis titrations of **AK-Z1, AK-Z2** and **AK-Z4** with ds- polynucleotides at pH = 7.0 (sodium cacodylate buffer, $I = 0.05$ mol dm^{-3}).

	ctDNA		AT-DNA		GC-DNA		AU-RNA	
	logK_s	H (%)[d]	logK_s	H (%)[d]	logK_s	H (%)[d]	logK_s	H (%)[d]
AK-Z1	5.7	6	-[c]	-[c]	5.8	9	5.0	13
AK-Z2	5.5	7	6.0	5	4.7	9	5.9	14
AK-Z4	5.8	17	6.0	25	5.9	34	6.3	30

[a,b] Processing of titration data using the Scatchard equation gave stability constants K_s; all K_s values were re-calculated with fixed value n([bound compound]/[polynucleotide phosphate]) = 0.2 for comparison reasons; correlation coefficients were >0.98 for all calculated K_s.

[c] A small total absorption change and high divergences of absorbance intensities enabled only the estimation of the stability constant.

[d] Hypochromic effect calculated by Scatchard for **AK-Z1**, **AK-Z2** and **AK-Z4** at λ_{max}; H = (Abs(**AK-Z1**, **AK-Z2** and **AK-Z4**) - Abs(complex))/Abs(**AK-Z1**, **AK-Z2** and **AK-Z4**) × 100.

region at λ > 300 nm, with distinct profiles for AT-DNA, GC-DNA, and AU-RNA. In the case of AU-RNA, two well-resolved exciton couplets were observed: a negative couplet in the aggregate absorption region centered at 591 nm and a positive couplet in the monomer region

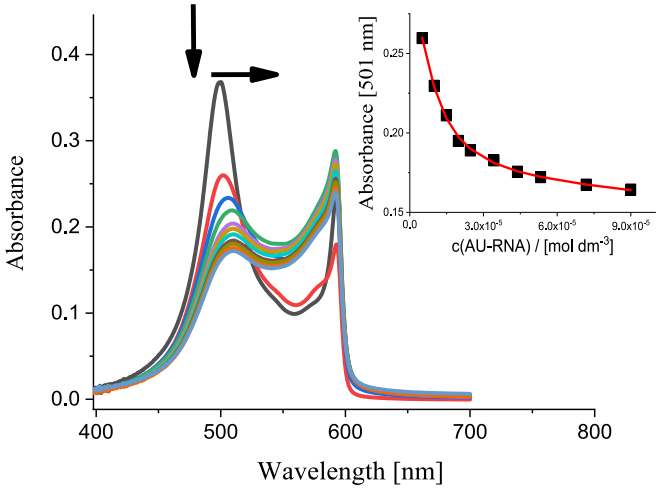


Fig. 3. Changes in UV/Vis spectrum of **AK-Z4** ($c = 5.0 \times 10^{-6}$ mol dm^{-3}, $\lambda_{abs} = 501$ nm) upon titration with AU-RNA ($c = 5.0 \times 10^{-6}$–9.0×10^{-5} mol dm^{-3}); Inset: Dependence of **AK-Z4** absorbance at $\lambda = 501$ nm on c(AU-RNA), at pH = 7, sodium cacodylate buffer, $I = 0.05$ mol dm^{-3}.

centered at 501 nm [37].

Similar spectral changes were seen for ctDNA and AT-DNA at low ligand-to-polynucleotide ratios ($r = 0.1$). However, at higher ratios ($r = 0.3$), the ICD signals associated with monomers and aggregates merged into a broader band. For GC-DNA, the monomer-associated ICD signal was absent, likely because the amino groups of guanine hinder ligand access to the minor groove [28]. To further evaluate the effect of the guanine amino group on **AK-Z4** monomer binding, we conducted experiments with poly(dIdC)·poly(dIdC) (IC-DNA), a close analogue of GC-DNA that lacks amino groups on the purine bases.

As expected, a monomer-associated signal appeared at 504 nm. However, it was not shown as a bisignate couplet but as a single negative ICD band, indicating that **AK-Z4** binds as a monomer within the minor groove of IC-DNA [38]. Interestingly, in the aggregate absorption region, a small positive exciton couplet was detected at a low ratio (r = 0.1), in contrast to the negative couplet observed for GC-DNA.

Exciton-coupled CD signals (bisignate ICD bands) indicate the formation of dimers or higher-order assemblies, occurring either through groove binding or external stacking on the DNA [38]. Armitage and colleagues proposed a model in which two dye molecules form a cofacial dimer within the DNA minor groove, with additional dimers aligned

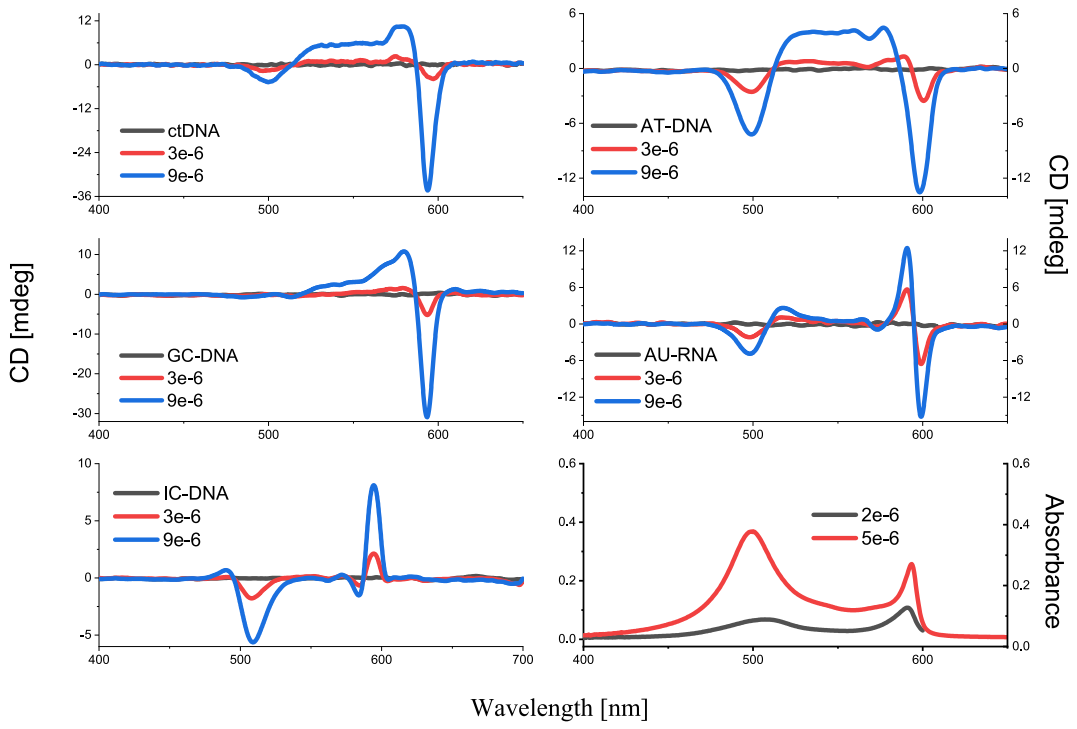


Fig. 4. CD titration of ctDNA, AT-DNA, GC-DNA, AU-RNA, IC-DNA ($c = 3.0 \times 10^{-5}$ mol dm^{-3}) with **AK-Z4** at indicated concentrations (pH = 7.0, sodium cacodylate buffer, $I = 0.05$ mol dm^{-3}); a part of the titration with the CD signals of polynucleotides is not shown for better visibility of the ICD signal (see in SI).

consecutively along the groove [35,36,39–41]. Coupling between neighbouring dimers results in exciton splitting and the appearance of characteristic positive and negative CD bands [42]. When the long-wavelength band is positive and the short-wavelength band is negative, as observed for the monomer-associated positive couplet of **AK-Z4**, the arrangement corresponds to a right-handed helical organization of adjacent dimers, consistent with the intrinsic right-handed helicity of DNA. In contrast, the aggregate-associated negative exciton couplet of **AK-Z4**, characterized by a negative long-wavelength band and a positive short-wavelength band, suggests the formation of a left-handed helical assembly of aggregated chromophores, opposite to the helicity of the DNA template [39].

An exception was observed for IC-DNA, where the positive exciton couplet indicates the formation of a right-handed helical arrangement of aggregated chromophores (Fig. 4).

Summarized results, including thermal melting studies, suggest that **AK-Z4** monomer/dimer species bind within the minor groove, aligning along its axis. J-aggregates probably bind along the major groove since the minor groove is already occupied.

2.3.4. *Interactions with G-quadruplex structures*

Interactions with G-quadruplex structures are studied using the Tel22 oligonucleotide (5′-AGGG(TTAGGG)$_3$-3′), a widely used model of telomeric G-quadruplex DNA [43]. In Na^+ solution, Tel22 adopts a basket-type intramolecular G-quadruplex with three stacked G-tetrads connected by two lateral TTA loops and one diagonal loop [44]. In the K^+ solution, Tel22 adopts mixed parallel/antiparallel or chair-type topologies, as shown by circular dichroism (CD) spectroscopy [45,46].

G-quadruplexes (G4) are non-canonical nucleic acid structures that form in guanine-rich regions of DNA and RNA via Hoogsteen hydrogen bonding between four coplanar guanines. Due to their important biological roles, G4 structures have attracted considerable interest as therapeutic targets in anticancer and antiviral drugs, and G4- binding ligands are increasingly explored for precision medicine applications [47,48].

Because certain cyanine dyes exhibit preferentially binding toward G-quadruplex over duplex DNA, we investigated the interactions of compounds with G-quadruplex structures [10,49]. Since only **AK-Z4** showed significant fluorescence changes with ds-DNA/RNA, its interactions with Tel22 were further examined in both Na^+ and K^+ solutions (Fig. 5, Figs. S32-S34). G-quadruplex structures formed in K^+ solution are considered more biologically relevant since intracellular potassium concentrations are higher than sodium concentrations [46].

For analysis of the titration data, fluorescence changes in the monomer emission region were given the greatest weight, due to the less well-defined nature of aggregate emission and the limited structural information available for aggregate species. The binding constants and

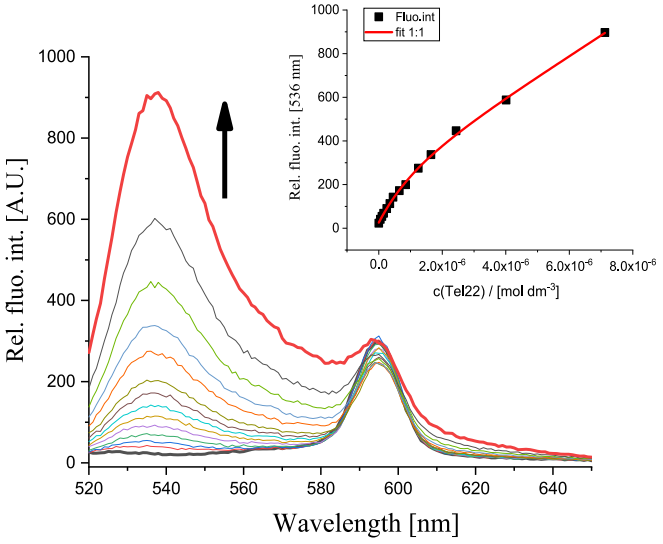


Fig. 5. Changes in fluorescence emission spectrum of **AK-Z4** ($c = 5.0 \times 10^{-7}$ mol dm^{-3}, $\lambda_{exc} = 501$ nm) upon titration with Tel22 ($c = 5.0 \times 10^{-8}$–7.1×10^{-6} mol dm^{-3}); Inset: Dependence of **AK-Z4** fluorescence at $\lambda = 536$ nm on c (Tel22), at pH = 7.0, potassium phosphate buffer, $I = 0.1$ mol dm^{-3}.

stoichiometry of the **AK-Z4**–Tel22 complex were determined using the non-linear least-squares fitting program SPECFIT [50]. The best fit corresponded to a 1:1 **AK-Z4**–Tel22 stoichiometry, and binding constants (log K_s) were calculated for both Na^+ and K^+ solutions (Table 4).

To further assess the selectivity of **AK-Z4** toward G-quadruplex structures, its binding was compared with the duplex-forming oligonucleotide ds26. However, fluorescence titration with ds26 showed a linear fluorescence response, preventing reliable nonlinear fitting and accurate determination of the binding constant. Based on these data, the binding constant was estimated to be lower than 10^5.

Comparison of the binding constants for **AK-Z4** with Tel22 (in both K^+ and Na^+ solutions) and ds26 reveals a preference for the G-quadruplex over duplex DNA, with the binding affinity for Tel22 approximately an order or two of magnitude higher than that estimated for duplex DNA. Selenium-substituted monomethine cyanines [10], styryl cyanines *N*-methylpiperazine and *N*-phenylpiperazine functionality [49] and phthalocyanines [51] showed similar selectivity toward the same G-quadruplex model. The binding affinities obtained for **AK-Z4** toward G-quadruplexes are consistent [10,49,51] with, or slightly lower [52,53] than, literature values reported for related G-quadruplex-binding dyes.

Similar to titration with AU-RNA polynucleotide, the addition of **AK-Z4** to Tel22 oligonucleotide in Na^+ solution produced two exciton couplets in the CD spectrum: a negative exciton couplet at 591 nm associated with J-aggregate and a positive couplet at 501 nm associated with monomer/dimer species (Fig. 6, Fig. S35). In the K^+ solution, the ICD profile of the G-quadruplex differed — at lower ratios ($r = 0.5$), the bisignate ICD signal was not visible. In contrast, at higher ratios, the J-aggregate couplet appeared slightly distorted, likely reflecting structural differences in the two G-quadruplex structures upon ligand binding. Fluorescence lifetime measurements further support the presence of multiple emissive populations in the **AK-Z4**–Tel22 complex (Table S2). Relative to free **AK-Z4**, which shows a dominant long-lived component of 6.82 ns, binding to Tel22 eliminates this long-lived species and produces decay profiles dominated by shorter components at approximately 1.5–1.6 ns and 2.6–3.3 ns (Tables S2 and S3). In parallel, the fluorescence quantum yield increases upon G-quadruplex binding, reaching 4.09% in Na^+ and 3.39% in K^+, indicating that complex formation alters the local dye environment and partially rigidifies the chromophore (Table S1). Considering the extended planar π-conjugated system of **AK-Z4** and the 1:1 binding stoichiometry determined for the **AK-Z4**–Tel22 complex, monomer binding via stacking interactions at the terminal G-quartets represents a reasonable and well-established binding mode for cyanine dyes. The observed exciton-coupled bisignate ICD signals suggest that dimers and J-aggregates interact with nucleobases or with the phosphate backbone in the grooves or loops of the G-quadruplex. Accurate determination of these interactions would require additional complex and time-consuming structural studies (e.g., NMR, X-ray crystallography, or molecular modelling), which are beyond the scope of the present work [54].

Table 4
Binding constants (logK_s)[a] for 1:1 complex of **AKZ4**-Tel22 calculated from the fluorescence titrations (sodium cacodylate buffer and potassium phosphate buffer, pH = 7.0, I = 0.1 mol dm^{-3}).

Buffer	Log K_s[b]
K^+	6.32 ± 0.07
Na^+	6.99 ± 0.18

[a] Stability constant log K_s and stoichiometry calculated by processing the titration data SPECFIT program.

[b] K_s refer to the equilibrium L + G⇆ LG (L = ligand, G = G-quadruplex).

Interestingly, despite the substantial differences in length and topology between double-stranded RNA and four-stranded G-quadruplex structures, the observed excitonic ICD signals are remarkably similar, though less intense for the G-quadruplex formed in Na^+ solution.

2.4. Interactions of AK-Z compounds with liposomes

The three dyes are incorporated into the bilayer of multilamellar lipid vesicles (MLV), where they act as fluorescent reporters of phase transitions through changes in emission. In this system, lipid bilayers serve as a model for biological membranes. The selected lipids, DPPC and DPPS (see Abbreviations in Experimental), mimic eukaryotic membranes, in which phosphatidylcholine (PC) lipids are predominantly located in the outer leaflet, whereas phosphatidylserine (PS) lipids are found on the inner (luminal) side of the bilayer [55]. Upon heating, the MLVs undergo pretransition from the gel phase to the ripple phase (T_p), followed by the main transition to the fluid phase (T_m) [56]. Monitoring these transitions in situ is important because the lipid phase state plays a key role in regulating membrane biological functions. Due to their high sensitivity and bioavailability, fluorescent probes are the best candidates for this task [57].

The two transition events in the MLV formulation without dyes are observed in the DSC thermogram (Fig. S36). At 2% dye concentration, the two monomethine dyes (**AK-Z1** and **AK-Z2**) do not considerably affect the transition events, as the onset temperatures of both the pretransition and main transition remain comparable to those of dye-free MLVs (Figs. S37 and S38). In contrast, the trimethine dye **AK-Z4** induces slight destabilisation of the bilayer, lowering the onset temperatures by approximately 1.5 °C (T_p) and 1.2 °C (T_m) (Fig. S39). As previously described, **AK-Z4** tends to form aggregates in the lipid bilayer environment. Such clustering within the bilayer likely disrupts van der Waals interactions between lipid molecules, providing a plausible explanation for the observed destabilisation. The MLV phase transitions were also monitored by temperature-dependent fluorescence measurements. Changes in the fluorescence intensity are recorded, and the spectra are deconvoluted using MCR-ALS with EFA (see abbreviations in experimental section). The results indicate that **AK-Z2** reports both T_p and T_m via changes in the emission, **AK-Z1** is primarily sensitive to the pretransition, and **AK-Z4** more effectively marks the main transition (Figs. S40-S43). These differences in reporting ability likely arise from a combination of factors, including aggregation/disaggregation, a localization within the bilayer, and the resulting local microenvironment.

The dyes incorporated into MLV were also checked for their fluorescence lifetime (Table S3 in SI). As observed previously, **AK-Z1** and **AK-Z2** exhibit short lifetimes in the solution. A similar behaviour is observed in MLVs. In contrast, the more complex lifetime behaviour of free **AK-Z4** is not observed within the bilayer, regardless of the phase. In both gel (20 °C) and fluid (50 °C) phases, all three dyes show relatively short fluorescence lifetimes ($\tau < 0.3$ ns).

3. Biological activity

3.1. MTT and AlamarBlue assays

The effects of compounds **AK-Z1**, **AK-Z2**, and **AK-Z4** on cell viability were evaluated using MTT and AlamarBlue assays in tumour cell lines of different origins and carboplatin (CBP) sensitivity including HeLa, SK-OV-3, MES-OV, and their CBP-resistant counterparts (SK-OV-3 CBP and MES-OV CBP). The CBP-resistant ovarian cancer cell lines have been previously characterized [58,59]. To assess selectivity, normal human fibroblasts were included, as an important criterion for potential antitumor agents is low toxicity toward normal cells combined with a non-selective effect across tumour cell lines. In addition, a lack of selectivity between drug-sensitive and drug-resistant cancer cells is considered favourable. Owing to differences in metabolic characteristics, growth behaviour, and assay sensitivity among the investigated cell lines, the

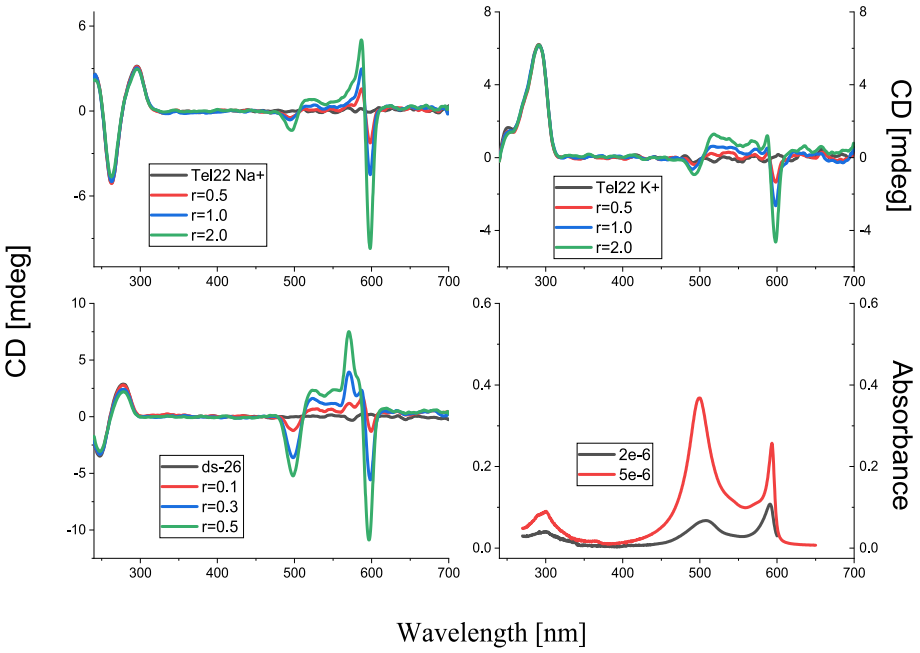


Fig. 6. CD titrations of ds-26 ($c = 2.0 \times 10^{-5}$ mol dm^{-3}, pH = 7.0, sodium cacodylate buffer, $I = 0.05$ mol dm^{-3}), Tel22(Na^+) ($c = 1.5 \times 10^{-6}$ mol dm^{-3}, pH = 7.0, sodium cacodylate buffer, $I = 0.1$ mol dm^{-3}) and Tel22(K^+) ($c = 1.5 \times 10^{-6}$ mol dm^{-3}, pH = 7.0, potassium phosphate buffer (K^+), $I = 0.1$ mol dm^{-3}) with **AK-Z4** at molar ratios $\boldsymbol{r}$ = [compound] / [nucleotide] and UV/Vis spectra of **AK-Z4**.

MTT assay was used to assess compound effects on the viability of HeLa cells and fibroblasts, while the AlamarBlue assay was applied to ovarian cancer cell lines (SK-OV-3 and MES-OV pairs). The IC_{50} values obtained after 72 h incubation are summarized in Table 5. Among the tested compounds, **AK-Z4** showed the strongest cytotoxic effect against HeLa cell line, while **AK-Z1** was most active against MES-OV cell line. However, **AK-Z4** also exhibited high toxicity toward normal fibroblasts (see Figs. S44–46 in the SI), whereas **AK-Z1** had significantly lower effects on fibroblasts, making it the more promising candidate for further investigation. Importantly, none of the compounds exhibited greater toxicity toward CBP-resistant cells than their parental counterparts; in all cases, the resistant cells were less sensitive. The observed IC_{50} values fall within the range reported previously for similar cyanine dyes [10], although in some cases these compounds exhibited slightly lower potencies [5,8,10].

3.2. Confocal microscopy

Confocal microscopy enables the visualization and localization of **AK-Z1**, **AK-Z2** and **AK-Z4** within the cell. All compounds enter HeLa cells after 60 min of incubation at a 5 micromolar concentration (Fig. 7).

AK-Z4 predominantly accumulates in mitochondria, in agreement with literature reports [13,60]. Mitochondrial localization was confirmed using the commercial probe MitoTracker Deep Red (Fig. 8). Co-localization analysis, based on Pearson's correlation coefficient (PCC) [61] and corrected for noise using replicate-based noise correction correlation (RBNCC) [62], yielded a value of 0.798, indicating strong mitochondrial targeting (Fig. 8, Fig. S48a). Furthermore, fluorescence intensity distribution curves (Fig. S48), obtained from mitochondria-defined regions of interest (ROIs) by thresholding the MitoTracker signal and applying the same regions to both channels, showed partially overlapping normalized profiles. This observation is consistent with the high PCC value and further supports mitochondrial localization.

AK-Z1 showed partial localization in both mitochondria and the endoplasmic reticulum, as as supported by co-localization analysis with MitoTracker Deep Red and a commercial endoplasmic reticulum (ER)-Tracker Red (Figs. S49-S50). PCC analysis gave values of 0.694 for mitochondria and 0.629 for the ER, indicating a dual intracellular distribution rather than specific organelle targeting.

For **AK-Z2**, PCC value could not be reliably determined due to its significantly weaker fluorescence intensity. Nevertheless, as shown in the image (Fig. S47 in the SI), the distribution of **AK-Z2** only partially overlaps with MitoTracker, indicating that part of the dye localizes in mitochondria, while the remainder is distributed in other cellular organelles, excluding the nucleus, which was proved with Hoechst 33342, a standard nuclear dye. The strong mitochondrial accumulation of **AK-Z4** is most likely a consequence of its enhanced charge delocalization and lipophilicity, arising from the combined effects of the extended trimethine bridge, benzimidazole core, and alkyl substitution, which together promote electrostatic accumulation within the negatively polarized mitochondrial membrane. In contrast, the less conjugated monomethine dyes **AK-Z1** and **AK-Z2** differ not only in bridge length but also in heterocyclic core (benzoxazole and benzothiazole, respectively) and substituents, all of which modulate lipophilicity independently of chain length and likely contribute to their reduced mitochondrial accumulation and more diffuse intracellular distribution.

Table 5
The cytotoxic activity of analysed compounds toward HeLa, SK-OV-3, SK-OV-3 CBP, MES-OV and MES-OV CBP cells and fibroblasts. IC_{50} (IC_{50}/μM) values were calculated after 72 h of incubation with the compounds. Cytotoxicity was measured by either the MTT assay (HeLa cells and fibroblasts) or the AlamarBlue assay (SK-OV-3 and MES-OV cell line pairs).

	IC_{50} (μM)		
	AK-Z1	AK-Z2	AK-Z4
Hela	17.69 ± 2.2	>30	1.65 ± 0.4
Fibroblasts	>20	>20	1.02 ± 0.1
SK-OV-3	29.12 ± 3.3	>30	28.62 ± 3.3
SK-OV-3 CBP	>30	>30	>40
MES-OV	3.63 ± 8.2	>30	27.92 ± 14.6
MES-OV CBP	13.31 ± 1.9	>30	14.77 ± 3.7

3.3. Antibacterial activity

All tested compounds demonstrated significant antibacterial activity

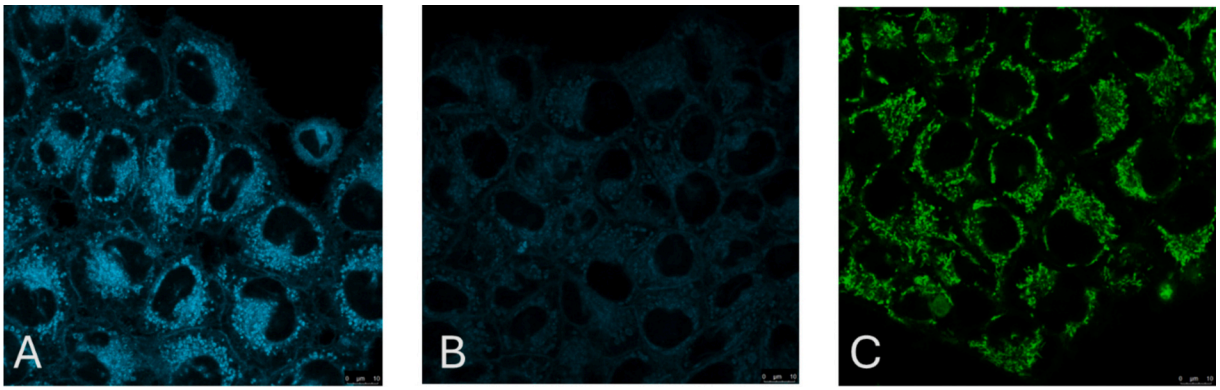


Fig. 7. Intracellular distribution of **AK-Z1** (A), **AK-Z2** (B) and **AK-Z4** (C). Confocal microscopy of live HeLa cells taken on Leica SP8 X confocal microscope, stained with 5 μM of tested compounds (λ_{exc} = 377, 401 and 501 nm, λ_{em} = 420–600 nm).

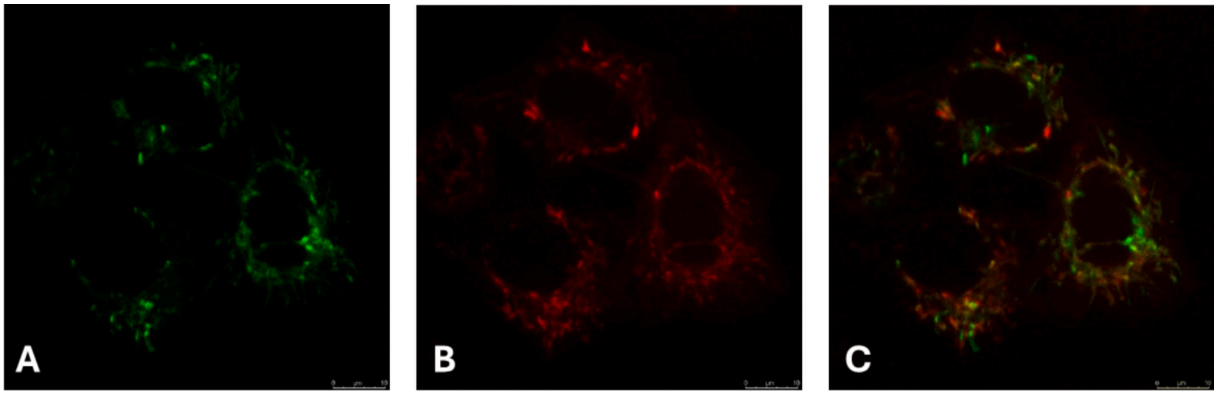


Fig. 8. Intracellular distribution of dye **AK-Z4** compared to MitoTracker. Confocal microscopy of live HeLa cells taken on Leica SP8 X confocal microscope, stained with 3 μM of compounds **AK-Z4**; A) channel showing emission of **AK-Z4** (λ_{exc} = 405 nm, λ_{em} = 470–670 nm); B) MitoTracker channel (λ_{exc} = 644 nm, λ_{em} = 665-700 nm); C) overlay of the two channels. Colocalization correlation, PCC values corrected for noise by the RBNCC method for **AK-Z4**.

against the Gram-positive strain *Staphylococcus aureus* ATCC 29213 (Table 6), with AK-Z1 showing the highest potency (MIC = 2.0 μg/mL), comparable to ampicillin. In contrast, their activity against Gram-negative strains (*Escherichia coli* ATCC 25922, *Escherichia coli* NCTC 13846 and *Pseudomonas aeruginosa* ATCC 27853) was markedly reduced or absent, which may be attributed to the limited permeability of the complex cell wall and the hydrophobic character of the heteroaromatic scaffold [63]. Unlike Gram-negative bacteria, *S. aureus* lacks the outer lipopolysaccharide layer, making it more permeable to large hydrophobic molecules, despite having a thicker peptidoglycan layer. The antibacterial activities observed generally align with previously reported data, in some cases higher, comparable, or lower, depending on the specific bacterial strain tested. Notably, the activity against *S. aureus* [64,65] exceeds that of similar benzooxazole-, benzothiazole-, and benzoimidazole-substituted compounds. In contrast, the activity against *E. coli* and *P. aeruginosa* is comparable to [65,66] or lower [64] than that of the compounds tested here.

Table 6
In vitro antibacterial activity of **AK-Z1, AK-Z2** and **AK-Z4** against Gram-positive and Gram-negative bacteria, expressed as MIC and MBC values (μg/mL).

MIC[a]	*S. aureus*	*E. coli ATCC*	*E. coli NCTC*	*P. aeruginosa*
AK-Z1	2.0	128	256	>256
AK-Z2	8.0	256	>256	>256
AK-Z4	16.0	>256	>256	>256
Ampicillin	1.0			
Ciprofloxacin		0.016	128	0.25
MBC[b]				
AK-Z1	32.0	128	>256	>256
AK-Z2	32.0	>256	>256	>256
AK-Z4	32.0	>256	>256	>256

[a] minimum inhibitory concentration;
[b] minimum bactericidal concentration.

MBC/MIC analysis further indicated a compound-dependent distinction between bacteriostatic and bactericidal behaviour [67]. **AK-Z1** was bacteriostatic against *S. aureus* but bactericidal against *E. coli* ATCC, whereas **AK-Z2** and **AK-Z4** displayed bactericidal activity against *S. aureus*.

Overall, the compounds showed a clear preference for Gram-positive bacteria. At the same time, the reference antibiotics remained substantially more potent, indicating that the tested compounds should currently be regarded as lead structures for further optimization rather than direct antimicrobial candidates. Among them, **AK-Z1** was selected as the most promising candidate because it displayed bacteriostatic activity against *S. aureus* and bactericidal activity against *E. coli* ATCC, suggesting that its activity could be further improved and broadened through structural modification, particularly against Gram-positive bacteria.

4. Conclusion

In this study, three chlorinated cyanine dyes were synthesized - two asymmetric monomethine derivatives (**AK-Z1, AK-Z2**) and one trimethine benzimidazole dye (**AK-Z4**). In addition to the difference in the bridge connecting the two aromatic moieties, further structure variations arise from the nature of the second aromatic ring (benzoxazole, benzothiazole, or benzimidazole) and from the presence of alkyl substituents on the aromatic ring (ethyl vs. S-propyl thioacetate).

Spectroscopic analyses showed that all dyes are stable and fluorescent in aqueous buffer, with **AK-Z4** exhibiting complex, temperature-dependent monomer–J aggregate equilibria, unlike the monomeric **AK-Z1** and **AK-Z2**.

AK-Z1 and **AK-Z2** interacted moderately and non-specifically with ds-DNA/RNA, resulting in weak thermal stabilisation and no induced CD signals, consistent with external binding. In contrast, **AK-Z4** showed a selective response to ds-RNA. It binds ds-DNA and ds-RNA with comparable affinity but displays a unique dual fluorimetric signature with AU-RNA, indicating the formation of both monomeric and aggregated complexes. ICD spectra revealed that **AK-Z4** forms well-defined monomer/dimer species in the minor groove and J-aggregate assemblies along the backbone or major groove, with helical arrangements dependent on the nucleic-acid structure. Of particular interest is the change in helical arrangement of adjacent dimers between GC- and IC-DNA (opposite-handed exciton couplets for GC- vs. IC-DNA). Furthermore, **AK-Z4** showed a clear preference for the Tel22 G-quadruplex over duplex DNA and produced topology-dependent ICD profiles in Na^+ and K^+ solutions. Taken together, these findings demonstrate that **AK-Z4** is highly sensitive to secondary-structure variations in both ds- and G-quadruplex nucleic acids, exhibiting a level of spectral discrimination previously reported only for one group of cyanines of this class, namely selenium-substituted monomethine cyanines [10]. These binding differences can be rationalized by structural features of the dyes. The extended trimethine bridge in **AK-Z4** enhances π-conjugation and molecular planarity, promoting stronger π–π stacking interactions and aggregation, and thereby enabling more defined and structure-sensitive binding modes toward nucleic acids. In contrast, the weak interactions of **AK-Z1** and **AK-Z2** with ds-DNA and ds-RNA, evidenced by negligible thermal stabilisation and absence of induced CD signals, are consistent with electrostatic surface binding lacking defined orientational order. This behaviour likely reflects their substituent pattern and monomethine scaffold, which disfavour the planar, self-associating geometry required for intercalation or groove binding. In lipid bilayers, all three dyes were incorporated into DPPC/DPPS multilamellar vesicles and reported on thermally induced phase transitions through changes in fluorescence emission. **AK-Z1** and **AK-Z2** minimally affected membrane thermodynamics, whereas **AK-Z4** slightly destabilised the bilayer, likely due to aggregation within the hydrophobic core. Despite their differing behaviours in solution, all dyes displayed similarly short fluorescence lifetimes when embedded in membranes, indicating environment-induced quenching and suggesting well-defined localization within the bilayer.

Biological evaluation showed that **AK-Z4** exhibited the strongest cytotoxicity toward tumour cells but lacked selectivity over normal fibroblasts. Compound **AK-Z1** demonstrated strong cytotoxic activity against the MES-OV cell line and a noticeably weaker effect on normal fibroblasts, highlighting its potential as a more selective candidate for further investigation.

Co-localization of **AK-Z4** with a mitochondrial tracker confirms its mitochondrial accumulation, consistent with its higher charge delocalization and lipophilicity arising from the trimethine bridge and substituents, which promote accumulation in the negatively polarized mitochondrial interior. Antibacterial assays revealed high potency against Gram-positive *S. aureus*, particularly for **AK-Z1**, whose activity was comparable to that of ampicillin, whereas activity against Gram-negative bacteria remained limited, most likely due to membrane impermeability. The favourable combination of molecular size, lipophilicity, and charge distribution in **AK-Z1** likely underlies its strong antibacterial activity against Gram-positive *S. aureus*, in contrast to the bulkier, aggregation-prone **AK-Z4** and the more polarisable benzothiazole analogue **AK-Z2**.

These results highlight **AK-Z4** as a structurally responsive nucleic acid probe that discriminates between DNA and RNA topologies through both fluorescence and ICD signatures, and identify **AK-Z1** as the most balanced candidate for further biological development due to its favourable antibacterial profile, moderate cytotoxicity, and selectivity over a normal cell line.

The combined spectroscopic, biophysical, and biological data emphasize the potential of chlorinated cyanine dyes as multifunctional agents for nucleic-acid sensing, membrane studies, and biomedical applications.

5. Materials and methods

5.1. Materials and synthetic methods

All solvents employed for synthesis and purification, including 5,6-Dichloro-1-ethyl-2-methylbenzimidazole (TCI, CAS: 3237-62-5, >98.0%), Iodoethane (Alfa Aesar, CAS: 75-03-6, 98 + %), Acetic anhydride (Sigma Aldrich, CAS: 108-24-7,99.5%), *N*,*N*-Diisopropylethylamine – DIPEA (Alfa Aesar, CAS: 7087-68-5, 99.5 + %), Potassium iodide (Sigma Aldrich, CAS: 7681-11-0, ACS reagent, ≥99.0%), Triethyl orthoformate (Alfa Aesar, CAS: 122-51-0,98%), 1,2-Dichlorobenzene (Alfa Aesar, CAS: 95-50-1, 99%) were used as received without further purification. Silica gel (high-purity grade, pore size 60 Å, 230–400 mesh particle size, 40–63 μm particle size, for flash chromatography) employed for the column chromatography was purchased from Sigma Aldrich.

The chemical identities of the compounds under investigation were verified through the application of various analytical techniques, including ^{1}H-NMR, ^{13}C NMR, and DEPT-135 spectroscopy. The spectra were obtained using a Bruker Avance II + 600 spectrometer (Institute of Organic Chemistry with Centre of Phytochemistry - Bulgarian Academy of Sciences/NMR Centre) employing 5 mm tubes. The measurements were conducted in DMSO-d_6 at 298 K, utilizing operating frequencies of 600.13 MHz and 150.92 MHz for the ^{1}H and ^{13}C nuclei, respectively. The ^{1}H- and ^{13}C- NMR spectra were calibrated using the reference signal of DMSO-d_6, with a chemical shift value (δ) of 2.50 ppm for the ^{1}H NMR and 39.52 ppm for the ^{13}C NMR, respectively. The accuracy of chemical modifications is established at a level of 0.01 ppm. The coupling constants (J) are expressed with a precision of 0.1 and are indicated in units of hertz (Hz). The spin multiplicity observed in the ^{1}H NMR spectroscopy was denoted using the following abbreviations: s for singlet, d for doublet, t for triplet, q for quartet, dd for doublet of doublets, dt for doublet of triplets, td for triplet of doublets, and m for multiplet. MestreNova version 14.1.1 (Mestrelab Research S.L.) was employed for spectral processing.

3-(3-(acetylthio)propyl)-2-((5,6-dichloro-1,3-diethyl-1,3-dihydro-2H-benzo[d]imidazol-2-ylidene)methyl)benzo[d]oxazol-3-ium iodide (**AK-Z1**) (Figs. S51-S64, Fig. S87):

^{1}H NMR (600 MHz, DMSO-d_6) δ 8.29 (s, 2H), 7.54 (d, J = 7.9 Hz, 1H), 7.50 (dd, J = 8.3, 1.0 Hz, 1H), 7.38 (td, J = 7.8, 0.9 Hz, 1H), 7.25 (td, J = 7.9, 1.1 Hz, 1H), 5.27 (s, 1H), 4.41 (q, J = 7.1 Hz, 4H), 4.26 (t, J = 6.8 Hz, 2H), 3.03–2.98 (m, 2H), 2.31 (s, 3H), 2.06 (p, J = 6.9 Hz, 2H), 1.42 (t, J = 7.2 Hz, 6H). ^{13}C NMR (151 MHz, DMSO-d_6) δ 195.3, 159.1, 150.7, 145.6, 131.7, 131.3, 127.6, 125.3, 123.2, 113.6, 110.0, 109.7, 54.0, 42.2, 41.4, 30.6, 27.00, 25.5, 13.5; HRMS (positive ion mode) m/z calculated for $C_{24}H_{26}Cl_2N_3O_2S$ $[M]^+$ 490.1117, found 490.1119.

3-(3-(acetylthio)propyl)-2-((5,6-dichloro-1-ethyl-3-methyl-1,3-dihydro-2H-benzo[d]imidazol-2-ylidene)methyl)benzo[d]thiazol-3-ium iodide (**AK-Z2**) (Figs. S65-S77, Fig. S88):

^{1}H NMR (600 MHz, DMSO-d_6) δ 8.37 (s, 1H), 8.32 (s, 1H), 7.79 (dd, J = 7.8, 1.0 Hz, 1H), 7.51 (d, J = 7.8 Hz, 1H), 7.47 (ddd, J = 8.3, 7.3, 1.2 Hz, 1H), 7.27–7.23 (m, 1H), 5.79 (s, 1H), 4.43 (q, J = 7.1 Hz, 2H), 4.32 (t, J = 7.2 Hz, 2H), 3.86 (s, 3H), 3.01 (m, 2H), 2.33 (s, 3H), 2.04 (p, J = 7.4 Hz, 2H), 1.32 (t, J = 7.2 Hz, 3H). ^{13}C NMR (151 MHz, DMSO-d_6) δ 195.3, 158.7, 152.6, 140.7, 132.7, 130.8, 128.2, 127.8, 127.5, 123.4, 122.8, 122.5, 114.4, 113.8, 111.5, 67.8, 44.0, 41.1, 40.1, 34.6, 30.6, 26.2, 25.6, 13.8; HRMS (positive ion mode) m/z calculated for $C_{23}H_{24}Cl_2N_3OS_2$ $[M]^+$ 492.0732, found 492.0730.

5,6-dichloro-2-(3-(5,6-dichloro-1,3-diethyl-1,3-dihydro-2H-benzo[d]

imidazol-2-ylidene)prop-1-en-1-yl)-1,3-diethyl-1H-benzo[d]imidazol-3-ium iodide (**AK-Z4**) (Figs. S78-S86, Fig. S89):

^{1}H NMR (600 MHz, DMSO-d_6) δ 8.01 (s, 4H), 7.83 (t, J = 13.4 Hz, 1H), 5.94 (d, J = 13.4 Hz, 2H), 4.32 (q, J = 7.2 Hz, 8H), 1.37 (t, J = 7.2 Hz, 12H). ^{13}C NMR (151 MHz, DMSO-d_6) δ 148.5, 142.1, 131.7, 126.00, 111.2, 85.5, 51.4, 40.1, 13.3; 7.1; HRMS (positive ion mode) m/z calculated for C25H27Cl4N4 $[M]^+$ 523.0984, found 523.0980.

5.2. Materials and spectrophotometric methods

5.2.1. Interactions with DNA/RNA

The UV/vis spectra were recorded on a Varian Cary 100 Bio spectrophotometer (Agilent, Santa Clara, CA, USA), CD spectra on JASCO J815 spectrophotometer (ABL&E Handels GmbH, Wien, Austria) and fluorescence spectra on a Varian Cary Eclipse spectrophotometer (Agilent, Santa Clara, CA, USA) at 25 °C using appropriate 1 cm path quartz cuvettes. Absolute quantum yields were determined using software implemented with the instrument by the Integrating sphere SC-30 of the Edinburgh FS5 spectrometer in the quartz cuvette of 10 mm path length, to avoid the scattering of incident light at the liquid-air interface, testing solutions with a 2 mL volume were used [68]. Fluorescence lifetime measurements were also done on the Edinburgh FS5 spectrometer.

Materials. Polynucleotides were purchased as noted: poly A–poly U, calf thymus ctDNA, poly(dAdT)$_2$, poly(dGdC)$_2$ and poly(dIdC)$_2$ (Sigma-Aldrich, St. Louis, MI, USA). Polynucleotides were dissolved in sodium cacodylate buffer, I = 0.05 mol dm^{-3}, pH = 7.0. The calf thymus ctDNA was additionally sonicated and filtered through a 0.45 mm filter [69]. Polynucleotide concentration was determined spectroscopically as the concentration of phosphates [70]. Spectrophotometric titrations were performed at pH = 7.0 (I = 0.05 mol dm^{-3}, sodium cacodylate buffer) by adding aliquots of polynucleotide solution into the solution of the studied compound for fluorimetric experiments and CD experiments were done by adding aliquots of the compound stock solution into the solution of a polynucleotide. In fluorimetric experiments excitation wavelength of λ_{exc} = 377, 401, and 501 nm was used to avoid the inner filter effect caused by increasing absorbance of the polynucleotide. Emission was collected in the range λ_{em} = 500–700 nm. Values for K_s obtained by processing titration data using the Scatchard equation [32,33], all have satisfactory correlation coefficients ($\geq$0.98).

Thermal melting curves for DNA, RNA and their complexes with studied compounds were determined as previously described by following the absorption change at 260 nm as a function of temperature. The absorbance of the ligands was subtracted from every curve, and the absorbance scale was normalized. T_m values are the midpoints of the transition curves determined from the maximum of the first derivative and checked graphically by the tangent method. The ΔT_m values were calculated by subtracting T_m of the free nucleic acid from T_m of the complex. Every ΔT_m value here reported was the average of two measurements. The error in ΔT_m is ±0.5 °C. 5′- AGGG(TTAGGG)$_3$–3’(Tel22) was obtained from IDT (Integrated DNA Technologies, Coralville, IA, USA). Tel22 was dissolved in 0.1 M either in sodium cacodylate or potassium phosphate buffer. The starting Tel22 oligonucleotide solution was first heated up to 95 °C for 10 min and then slowly cooled to 10 °C at the cooling rate of 1 °C/ min to allow DNA oligonucleotide to adopt a G-quadruplex structure. The G-quadruplex structure was confirmed by thermal melting and CD spectra [46]. The concentration of G quadruplex was expressed in terms of oligonucleotide structure. In fluorimetric titrations, aliquots of Tel 22 solution were added to the solution of ligand (c = 5 × 10^{-7} M, Figs. S32-S34 in SI).

5.2.2. Interactions with liposomes

5.2.2.1. Differential scanning calorimetry. 700 μL of the formulation consisting of dipalmitoylphosphatidylcholine (DPPC) and dipalmitoylphsphatidylserine (DPPS) lipids in a 9:1 ratio and 2% AK-Z dyes in 100 mM phosphate buffer (pH 7.3) with a final concentration of 5 mg/mL lipid content were used for DSC analysis. The calorimetric experiments were performed in Nano-DSC microcalorimeter, TA Instruments (New Castle, USA) at a scan rate of 1 °C min^{-1} and in the temperature range 10–90 °C (working cell volume is 300 μL). Prior to measurement, all the samples were degassed under reduced pressure. The samples were scanned in two independent experiments, in two heating-cooling cycles. After subtracting the buffer-buffer scan from the raw data, the baseline was manually constructed and subtracted from the curve. The phase transition temperatures of DPPC/DPPS multilamellar liposomes (pretransition, T_p and main transition T_m) were determined from the second heating run by reading the peak onsets.

5.2.2.2. Temperature dependent fluorescence analysis. The stock suspensions of MLV formulations with or without the 2% dyes present were diluted with 100 mM phosphate buffer pH 7.3 to achieve the concentration of lipids 0.125 mg/mL. Fluorescence spectra of the suspensions were acquired by Agilent Cary Eclipse spectrophotometer in the temperature range 30–60 °C, using 1 cm path length quartz cuvettes. The temperature increased by 1 °C and after 2 min equilibration, the fluorescence spectra were recorded using the following settings: free MLV: λ_{exc} = 380 nm, slit: 10–20 nm; MLV + **AK-Z1**: λ_{exc} = 377 nm, slit: 10–10 nm; MLV + **AK-Z2**: λ_{exc} = 401 nm, slit: 20–20 nm; MLV + **AK-Z4**: λ_{exc} = 501 nm, slit: 5–10 nm.

The temperature dependent fluorescence spectra of MLV with fluorescent probes were acquired in two independent experiments. Multivariate curve resolution with alternating least squares (MCR-ALS) [71] and evolving factor analysis (EFA) [72] resolves the problem of overlapping bands of the mixture components and the magnitude of spectral changes that occur because of external effects. Therefore, MCR-ALS with EFA was used in the determination of T_p and T_m of MLV with **AK-Z** dyes from their temperature dependent fluorescence spectra, as previously [18]. Resulting traces are marked in red in Figs. S37, S38, and S39.

5.3. Effect of AK-Z compounds on cell viability

5.3.1. Cell lines

Human cervical carcinoma HeLa (GIBCO BRL, Thermo Fisher Scientific, Grand Island, NY, USA), human ovarian adenocarcinoma SK-OV-3 and human ovarian cystadenocarcinoma MES-OV (ATCC-LGC Standards GmbH, Wesel, Germany) cell lines were purchased from the indicated cell culture banks. Carboplatin-resistant SK-OV-3 CBP and MES-OV CBP cell lines were established by Dr. Brozovic and were previously characterized [58,59]. Normal human skin fibroblasts were isolated from the upper arm of a 7-year old female donor at the Neurochemical Laboratory, Department of Chemistry and Biochemistry, School of Medicine, University of Zagreb. HeLa cells, and fibroblasts were grown in Dulbecco's Modified Eagle's Medium (DMEM; Sigma-Aldrich, USA) while SK-OV-3 and MES-OV cell line pairs were grown in McCoy's 5 A medium (Capricorn Scientific, Ebsdorfergrund, Germany). All media were supplemented with 10% fetal bovine serum (FBS; Sigma-Aldrich), 50 I.U./mL penicillin and 50 μg/mL streptomycin. Cells were cultured in a humidified atmosphere of 5% CO_2 at 37 °C and were subcultured every 3–4 days.

5.3.2. Cytotoxicity assay

HeLa, SK-OV-3, SK-OV-3 CBP, MES-OV, MES-OV CBP cells and fibroblasts were seeded in 96-well plates. Twenty-four hours later, the cells were treated in quadruplicate with different concentrations of compounds (dissolved in DMSO, kept at 4 °C and protected from light). After 72 h of incubation at 37 °C, the medium was aspirated and modified 3-(4,5-dimethylthiazol-2-yl)-2,5-diphenyltetrazolium bromide (MTT) [73] and AlamarBlue [74] assays were used to determine the cytotoxic effect of the tested compounds.

5.4. Co-localization assay

Live cell imaging was performed on the HeLa cell line treated with specific organic compounds. Adherent cells were maintained in a complete high glucose (4.5 g/L) Dulbecco's Modified Eagle's medium (DMEM, Sigma-Aldrich, Saint Louis, MO, USA) supplemented with 10% fetal bovine serum (FBS), 1% nonessential amino acids, and 1% antibiotic/antimycotic solution (all chemicals were purchased by Capricorn Scientific GmbH, Ebsdorfergrund, Germany). Cells were seeded in a 4-chamber 35 mm glass bottom dishes (IBL Baustoff+Labor GmbH, Gerasdorf bei Wien, Austria) at 1×10^4 cells per well, and cells were kept at 37 °C in 5% CO_2 in a HeraCell 150 humidified incubator (Heraeus, Hanau, Germany). Twenty-four hours later, the cells were treated with a 3 to 5 μM solution of AK-Z2 or AK-Z4 respectively and left in the cell incubator for next 24 h to allow the compound to enter the cells. After the incubation, MitoTracker Deep Red solution (Invitrogen, Molecular Probes, Eugene, Oregon) was added to the specific chambers at a final concetration of 20 nM while the final concentration of ER-Tracker Red (Invitrogen, Molecular Probes, Eugene, Oregon) was 1 μM. Simultaneously, Hoechst 33342 cell-permeable fluorescent dye (Invitrogen, Molecular probes, Eugene, Oregon) was added at a final concentration of 5 μM. Cells were double-stained and incubated for 30 min (37 °C, 5% CO_2), allowing MitoTracker and Hoechst passive diffusion into live cells. After incubation, the medium was replaced with 500 μL of the fresh medium to reduce the signal-to-background ratio. Untreated control cells were used to exclude the presence of foreign fluorescence.

Co-localization of compounds with Hoechst 33342 ($\lambda_{exc} = 350$ nm, $\lambda_{em} = 461$ nm) that stains nucleus, ER-Tracker Red ($\lambda_{exc} = 587$ nm, $\lambda_{em} = 615$ nm) and MitoTracker ($\lambda_{exc} = 644$ nm, $\lambda_{em} = 665$ nm) was then visualized and confirmed using laser-scanning Leica SP8 X confocal microscope (Leica Microsystems, Wetzlar, Germany). Images were processed in LAS X Leica Microsystems software packages using Photoshop CS5.

5.5. Antibacterial screening

Antibacterial susceptibility was determined against standard bacterial strains: Gram-positive *Staphylococcus aureus* (ATCC 29213) and Gram-negative *Escherichia coli* (ATCC 25922), *Escherichia coli* (NCTC 13846) and *Pseudomonas aeruginosa* (ATCC 27853). Minimum inhibitory concentrations (MICs) were determined by the broth microdilution method according to the guidelines of the Clinical Laboratory Standards Institute [75]. Two-fold serial dilutions of tested compounds and control antibiotics (Ampicillin, Ciprofloxacin, Sigma-Aldrich, Laramie, WY, USA) were prepared in 96-well microplates in the 256–0.04 μg mL − 1 concentration range in cation adjusted Mueller Hinton broth (Oxoid CM0405, Thermo Fisher Scientific, Basingstoke, England). Inocula were prepared by the direct colony suspension method and plates were inoculated with 5×10^4 CFU per well. MIC values were determined by visual inspection after 24 h of incubation at 37 °C in ambient air, while MBC values were assessed after 48 h total incubation.

CRediT authorship contribution statement

Nina Vukadinović: Methodology, Investigation, Formal analysis, Data curation. **Ivo Crnolatac:** Writing – original draft, Supervision, Investigation, Conceptualization. **Atanas Kurutos:** Writing – review & editing, Writing – original draft, Investigation, Funding acquisition, Conceptualization. **Petra Jadrijević-Mladar:** Methodology, Investigation. **Lidija-Marija Tumir:** Writing – review & editing, Supervision. **Anamaria Brozovic:** Writing – review & editing, Writing – original draft, Investigation, Funding acquisition, Conceptualization. **Ana Tomašić Paić:** Methodology, Formal analysis. **Lucija Horvat:** Methodology, Formal analysis. **Marijana Radić Stojković:** Writing – review & editing, Writing – original draft, Supervision, Investigation, Funding acquisition, Conceptualization.

Declaration of competing interest

The authors declare that they have no known competing financial interests or personal relationships that could have appeared to influence the work reported in this paper.

Acknowledgments

Financial support from the Croatian Science Foundation under the projects IP-2024-05-7701, IP-2022-10-5202 and DOK-NPOO-2023-10-7710 are gratefully acknowledged. The financial support by the Bulgarian National Science Fund (BNSF) under grant – "Novel styryl and polymethine fluorophores as potential theranostic agents" contract No КП-06-М59/1 from November 15, 2021 is gratefully acknowledged by A.K. This work is also developed and acknowledged by A.K. as part of contract No: BG-RRP-2.004-0002-C01, Laboratory of Organic Functional Materials (Project BiOrgaMCT), Procedure BG-RRP-2.004 „Establishing of a network of research higher education institutions in Bulgaria", funded by BULGARIAN NATIONAL RECOVERY AND RESILIENCE PLAN".

Appendix A. Supplementary data

Supplementary data to this article can be found online at https://doi.org/10.1016/j.bioorg.2026.110016.

Data availability

The raw data will be available in the repository at https://data.fulir.irb.hr/

References

[1] Zeno Simon, Nicolae Voiculetz, I. Motoc, Specific Interaction and Biological Recognition Processes, 1st ed., CRC Press, Boca Raton, 1993.
[2] M. Demeunynck, C. Bailly, W.D. Wilson, Small Molecule DNA and RNA Binders, Wiley-VCH, Weinheim, 2002.
[3] A. Fürstenberg, M.D. Julliard, T.G. Deligeorgiev, N.I. Gadjev, A.A. Vasilev, E. Vauthey, Ultrafast excited-state dynamics of DNA fluorescent intercalators: New insight into the fluorescence enhancement mechanism, J. Am. Chem. Soc. 128 (23) (2006) 7661–7669.
[4] B.A. Armitage, Cyanine dye-DNA interactions: intercalation, groove binding, and aggregation, Top. Curr. Chem. 253 (2005) 55–76.
[5] L. Glavas-Obrovac, I. Piantanida, S. Marczi, L. Masic, I.I. Timcheva, T. G. Deligeorgiev, Minor structural differences of monomethine cyanine derivatives yield strong variation in their interactions with DNA, RNA as well as on their in vitro antiproliferative activity, Bioorg. Med. Chem. 17 (13) (2009) 4747–4755.
[6] M.I. Kandinska, D.V. Cheshmedzhieva, A. Kostadinov, K. Rusinov, M. Rangelov, N. Todorova, S. Ilieva, D.P. Ivanov, V. Videva, V.S. Lozanov, S. Baluschev, K. Landfester, V. AA, Tricationic asymmetric monomeric monomethine cyanine dyes with chlorine and trifluoromethyl functionality – fluorogenic nucleic acids probes, J. Mol. Liq. 342 (2021) 117501.
[7] A. Biancardi, T. Biver, A. Marini, B. Mennucci, F. Secco, Thiazole orange (TO) as a light-switch probe: a combined quantum-mechanical and spectroscopic study, Phys. Chem. Chem. Phys. 13 (27) (2011) 12595–12602.
[8] I. Zonjić, A. Kurutos, P. Mihovilović, I. Crnolatac, L.M. Tumir, A. Tomašić Paić, J. Kralj, L. Horvat, A. Brozovic, R. Stojković, M. Radić Stojković, Formation of triplex rA/dA-containing nucleic acid helices induced by new thiazole orange analogues and their biological evaluation. H-aggregate formation conditioned by rA sequence, Dyes Pigments 207 (2022) 110715.
[9] A. Kurutos, N. Gadjev, T. Deligeorgiev, Synthesis of novel asymmetric monomethine cyanine dyes containing benzoselenazolyl moiety. Fluorescent dsDNA probes, Acta Sci. Nat. 2 (2015) 90–98.
[10] I. Fabijanic, A. Kurutos, A.T. Paic, V. Tadic, F.S. Kamounah, L. Horvat, A. Brozovic, I. Crnolatac, M.R. Stojkovic, Selenium-substituted monomethine cyanine dyes as selective G-Quadruplex spectroscopic probes with theranostic potential, Biomolecules 13 (1) (2023).
[11] V.B. Kovalska, V.P. Tokar, M.Y. Losytskyy, T. Deligeorgiev, A. Vassilev, N. Gadjev, K.H. Drexhage, S.M. Yarmoluk, Studies of monomeric and homodimeric oxazolo [4,5-b]pyridinium cyanine dyes as fluorescent probes for nucleic acids visualization, J. Biochem. Biophys. Methods 68 (3) (2006) 155–165.
[12] X. Ma, L. Shi, B. Zhang, L. Liu, Y. Fu, X. Zhang, Recent advances in bioprobes and biolabels based on cyanine dyes, Anal. Bioanal. Chem. 414 (16) (2022) 4551–4573.
[13] S.T. Smiley, M. Reers, C. Mottola-Hartshorn, M. Lin, A. Chen, T.W. Smith, G. D. Steele Jr., L.B. Chen, Intracellular heterogeneity in mitochondrial membrane

potentials revealed by a J-aggregate-forming lipophilic cation JC-1, Proc. Natl. Acad. Sci. USA 88 (9) (1991) 3671–3675.
[14] A. Cossarizza, M. Baccarani-Contri, G. Kalashnikova, C. Franceschi, A new method for the cytofluorimetric analysis of mitochondrial membrane potential using the J-aggregate forming lipophilic cation 5,5′,6,6′-tetrachloro-1,1′,3,3′-tetraethylbenzimidazolcarbocyanine iodide (JC-1), Biochem. Biophys. Res. Commun. 197 (1) (1993) 40–45.
[15] M. Reers, T.W. Smith, L.B. Chen, J-aggregate formation of a carbocyanine as a quantitative fluorescent indicator of membrane potential, Biochemistry 30 (18) (1991) 4480–4486.
[16] B. Chanda, M.K. Mathew, Functional reconstitution of bacterially expressed human potassium channels in proteoliposomes: membrane potential measurements with JC-1 to assay ion channel activity, Biochim. Biophys. Acta 1416 (1–2) (1999) 92–100.
[17] L. Sanchez-Aranguren, M.A. Al Tahan, M. Uppal, P. Juvale, M.K. Marwah, Mitochondrial-targeted liposome-based drug delivery - therapeutic potential and challenges, J. Drug Target. 33 (5) (2025) 575–586.
[18] Z. Brkljača, M. Ćehić, T. Portada, M. Butumović, D. Bakarić, I. Crnolatac, Monitoring lipid phase transition temperatures using fluorescent probes and temperature-dependent fluorescence spectroscopy, Dyes Pigments 206 (2022) 110621.
[19] A. Kurutos, J. Nikodinovic-Runic, A. Veselinovic, J.B. Veselinovic, F.S. Kamounah, T. Ilic-Tomic, RNA-targeting low-molecular-weight fluorophores for nucleoli staining: synthesis, modelling and cellular imaging, New J. Chem. 45 (29) (2021) 12818–12829.
[20] A. Kurutos, I. Orehovec, A.T. Paic, I. Crnolatac, L. Horvat, N. Gadjev, I. Piantanida, T. Deligeorgiev, New series of non-toxic DNA intercalators, mitochondria targeting fluorescent dyes, Dyes Pigments 148 (2018) 452–459.
[21] A.C. Benniston, A. Harriman, Photoisomerization of a sterically constrained merocyanine dye, J. Chem. Soc. Faraday T 94 (13) (1998) 1841–1847.
[22] B. Schade, A.K. Singh, V. Wycisk, J.L. Cuellar-Camacho, H. von Berlepsch, R. Haag, C. Böttcher, Stereochemistry-controlled supramolecular architectures of new tetrahydroxy-functionalised amphiphilic carbocyanine dyes, Chem. Eur. J. 26 (30) (2020) 6919–6934.
[23] J.D. Mee, Acetylenic analogs of the cyanine dyes. 2. Synthesis of isomeric acetylenic dyes, J. Organomet. Chem. 42 (6) (1977) 1035–1040.
[24] Z.H. Peng, H.J. Geise, X.F. Zhou, B.X. Peng, R. Carleer, R. Dommisse, The structure of benzimidazole cyanine dyes, their spectroscopy and their performance in photographic emulsions, Liebigs Ann./Recl. 1 (1997) 27–33.
[25] E.J.V. Lare, Symmetrical carbocyanine dyes, in: U.S.P.A.T. Office (Ed.), 1956.
[26] F. Koide, T. Nomoto, S. Yamauchi, K. Watanabe, T. Shintou, T. Miyazaki, Y. Tabata, E. Sanda, Macrophage Identification Agent, and Identification Method, Sorting Method, Evaluation Method, Screening Method and Kit Using the Macrophage Identifier Agent, 2014.
[27] E.E. Jelley, Molecular, nematic and crystal states of I: I-diethyl–cyanine chloride, Nature 139 (1937) 631.
[28] S. W., Principles of Nucleic Acid Structure, Springer-Verlag, New York, 1984.
[29] S. Neidle, Oxford Handbook of Nucleic Acid Structure, Oxford University Press, Oxford, UK, 1999.
[30] C.R. Cantor, Techniques for the Study of Biological Structure and Function, W. H. Freeman, San Francisco, 1980.
[31] J.L. Mergny, L. Lacroix, Analysis of thermal melting curves, Oligonucleotides 13 (6) (2003) 515–537.
[32] G. Scatchard, The attractions of proteins for small molecules and ions, Ann. N. Y. Acad. Sci. 51 (1949) 660–672.
[33] J.D. McGhee, P.H. von Hippel, Theoretical aspects of DNA-protein interactions: co-operative and non-co-operative binding of large ligands to a one-dimensional homogeneous lattice, J. Mol. Biol. 86 (2) (1974) 469–489.
[34] R. A., N. B., Circular Dichroism and Linear Dichroism, Oxford University Press, New York, NY, USA, 1997.
[35] M.M. Wang, G.L. Silva, B.A. Armitage, DNA-templated formation of a helical cyanine dye J-aggregate, J. Am. Chem. Soc. 122 (41) (2000) 9977–9986.
[36] C. Li, J.L. Chen, T.T. Man, B. Chen, J. Li, Q. Li, X.R. Yang, Y. Wan, C.H. Fan, J. L. Shen, DNA framework-engineered assembly of cyanine dyes for structural identification of nucleic acids, JACS Au 4 (3) (2024) 1125–1133.
[37] M. Eriksson, B. Norden, Linear and circular dichroism of drug-nucleic acid complexes, Methods Enzymol. 340 (2001) 68–98.
[38] T. Smidlehner, I. Piantanida, G. Pescitelli, Polarization spectroscopy methods in the determination of interactions of small molecules with nucleic acids - tutorial, Beilstein J. Org. Chem. 14 (2018) 84–105.
[39] M.A. Ustimova, Y.V. Fedorov, V.B. Tsvetkov, S.D. Tokarev, N.A. Shepel, O. A. Fedorova, Helical aggregates of bis(styryl) dyes formed by DNA templating, J. Photochem. Photobiol., A 418 (2021).
[40] R.A. Garoff, E.A. Litzinger, R.E. Connor, I. Fishman, B.A. Armitage, Helical aggregation of cyanine dyes on DNA templates: effect of dye structure on formation of homo- and heteroaggregates, Langmuir 18 (16) (2002) 6330–6337.
[41] A. Chowdhury, S. Wachsmann-Hogiu, P.R. Bangal, I. Raheem, L.A. Peteanu, Characterization of chiral H and J aggregates of cyanine dyes formed by DNA templating using stark and fluorescence spectroscopies, J. Phys. Chem. B 105 (48) (2001) 12196–12201.
[42] F. Würthner, T.E. Kaiser, C.R. Saha-Möller, J-aggregates: from serendipitous discovery to supramolecular engineering of functional dye materials, Angew. Chem. Int. Edit. 50 (15) (2011) 3376–3410.
[43] J.B. Chaires, Human telomeric G-quadruplex: thermodynamic and kinetic studies of telomeric quadruplex stability, FEBS J. 277 (5) (2010) 1098–1106.
[44] Y. Wang, D.J. Patel, Solution structure of the human telomeric repeat d[AG3 (T2AG3)3] G-tetraplex, Structure 1 (4) (1993) 263–282.
[45] A.T. Phan, V. Kuryavyi, K.N. Luu, D.J. Patel, Structure of two intramolecular G-quadruplexes formed by natural human telomere sequences in K+ solution, Nucleic Acids Res. 35 (19) (2007) 6517–6525.
[46] Y. Xu, Y. Noguchi, H. Sugiyama, The new models of the human telomere d[AGGG (TTAGGG)3] in K+ solution, Bioorg. Med. Chem. 14 (16) (2006) 5584–5591.
[47] S.L. Cree, M.A. Kennedy, Relevance of G-quadruplex structures to pharmacogenetics, Front. Pharmacol. 5 (2014) 160.
[48] D.J. Patel, A.T. Phan, V. Kuryavyi, Human telomere, oncogenic promoter and 5'-UTR G-quadruplexes: diverse higher order DNA and RNA targets for cancer therapeutics, Nucleic Acids Res. 35 (22) (2007) 7429–7455.
[49] I. Zonjic, M.R. Stojkovic, I. Crnolatac, A.T. Paic, S. Psenicnik, A. Vasilev, M. Kandinska, M. Mondeshki, S. Baluschev, K. Landfester, L. Glavas-Obrovac, M. Jukic, J. Kralj, A. Brozovic, L. Horvat, L.M. Tumir, Styryl dyes with -Methylpiperazine and N-Phenylpiperazine functionality: AT-DNA and G-quadruplex binding ligands and theranostic agents, Bioorg. Chem. 127 (2022).
[50] H. Gampp, M. Maeder, C.J. Meyer, A.D. Zuberbuhler, Calculation of equilibrium constants from multiwavelength spectroscopic data–II: SPECFIT: two user-friendly programs in basic and standard FORTRAN 77, Talanta 32 (4) (1985) 257–264.
[51] C.I.V. Ramos, S.P. Almeida, L.M.O. Lourenço, P.M.R. Pereira, R. Fernandes, M.A. F. Faustino, J.P.C. Tomé, J. Carvalho, C. Cruz, M.G.P.M.S. Neves, Multicharged Phthalocyanines as selective ligands for G-Quadruplex DNA structures, Molecules 24 (4) (2019).
[52] S.B. Chen, J.H. Tan, T.M. Ou, S.L. Huang, L.K. An, H.B. Luo, D. Li, L.Q. Gu, Z. S. Huang, Pharmacophore-based discovery of triaryl-substituted imidazole as new telomeric G-quadruplex ligand, Bioorg. Med. Chem. Lett. 21 (3) (2011) 1004–1009.
[53] J. Zhou, V. Le, D. Kalia, S. Nakayama, C. Mikek, E.A. Lewis, H.O. Sintim, Diminazene or berenil, a classic duplex minor groove binder, binds to G-quadruplexes with low nanomolar dissociation constants and the amidine groups are also critical for G-quadruplex binding, Mol. BioSyst. 10 (10) (2014) 2724–2734.
[54] N.H. Campbell, G.N. Parkinson, A.P. Reszka, S. Neidle, Structural basis of DNA quadruplex recognition by an acridine drug, J. Am. Chem. Soc. 130 (21) (2008) 6722–6724.
[55] P.F. Devaux, Static and dynamic lipid asymmetry in cell-membranes, Biochemistry 30 (5) (1991) 1163–1173.
[56] R. Koynova, M. Caffrey, Phases and phase transitions of the phosphatidylcholines, Bba-Rev Biomembr. 1376 (1) (1998) 91–145.
[57] A.P. Demchenko, Y. Mély, G. Duportail, A.S. Klymchenko, Monitoring biophysical properties of lipid membranes by environment-sensitive fluorescent probes, Biophys. J. 96 (9) (2009) 3461–3470.
[58] J. Kralj, M.P. Kovac, S. Dabelic, D.S. Polancec, T. Wachtmeister, K. Köhrer, A. Brozovic, Transcriptome analysis of newly established carboplatin-resistant ovarian cancer cell model reveals genes shared by drug resistance and drug-induced EMT, Br. J. Cancer 128 (7) (2023) 1344–1359.
[59] M.P. Kovac, V. Tadic, J. Kralj, G.E. Duran, A. Stefanelli, D.S. Polancec, S. Dabelic, N. Bacic, M.T. Tomicic, P. Heffeter, B.I. Sikic, A. Brozovic, Carboplatin-induced upregulation of pan β-tubulin and class III β-tubulin is implicated in acquired resistance and cross-resistance of ovarian cancer, Cell. Mol. Life Sci. 80 (10) (2023).
[60] C.W. Hsieh, W.Y. Yang, Triggering Mitophagy with photosensitizers, Methods Mol. Biol. 1880 (2019) 611–619.
[61] K.W. Dunn, M.M. Kamocka, J.H. McDonald, A practical guide to evaluating colocalization in biological microscopy, Am. J. Phys. Cell Phys. 300 (4) (2011) C723–C742.
[62] J. Adler, S.N. Pagakis, I. Parmryd, Replicate-based noise corrected correlation for accurate measurements of colocalization, J. Microsc. 230 (Pt 1) (2008) 121–133.
[63] L. Brown, J.M. Wolf, R. Prados-Rosales, A. Casadevall, Through the wall: extracellular vesicles in gram-positive bacteria, mycobacteria and fungi, Nat. Rev. Microbiol. 13 (10) (2015) 620–630.
[64] V. Rep, R. Stulic, S. Kostrun, B. Kuridza, I. Crnolatac, M.R. Stojkovic, H.C. Paljetak, M. Peric, M. Matijasic, S. Raic-Malic, Novel tetrahydropyrimidinyl-substituted benzimidazoles and benzothiazoles: synthesis, antibacterial activity, DNA interactions and ADME profiling, RSC Med. Chem. 13 (12) (2022) 1504–1525.
[65] F. Nourmohammadian, M.Y. Alikhani, M.D. Gholami, A.A. Abdi, Benzothiazole-based Bis-azo cationic fluorescent dyes with extended conjugated systems: synthesis and properties, J. Appl. Sol. Chem. Model. 4 (2) (2015) 83–94.
[66] V.S. Padalkar, B.N. Borse, V.D. Gupta, K.R. Phatangare, V.S. Patil, P.G. Umape, N. Sekar, Synthesis and antimicrobial activity of novel 2-substituted benzimidazole, benzoxazole and benzothiazole derivatives, Arab. J. Chem. 9 (2016) S1125–S1130.
[67] E. Vaisbourd, D.S. Glass, Y.F. Yang, A. Mayo, A. Bren, U. Alon, Principles of bacteriostatic and bactericidal antibiotics at subinhibitory concentrations, mBio 16 (11) (2025).
[68] M. Koscak, I. Krosl, B. Zinic, I. Piantanida, Fluorescent analogues of FRH peptide: cu(II) binding and interactions with ds-DNA/RNA, Chemosensors 10 (1) (2022).
[69] J.B. Chaires, N. Dattagupta, D.M. Crothers, Studies on interaction of anthracycline antibiotics and deoxyribonucleic acid: equilibrium binding studies on interaction of daunomycin with deoxyribonucleic acid, Biochemistry 21 (17) (1982) 3933–3940.
[70] J.L. Bresloff, D.M. Crothers, Equilibrium studies of ethidium-polynucleotide interactions, Biochemistry 20 (12) (1981) 3547–3553.
[71] A. de Juan, J. Jaumot, R.A. Tauler, Multivariate curve resolution (MCR). Solving the mixture analysis problem, Anal. Methods-UK 6 (14) (2014) 4964–4976.

[72] J. Felten, H. Hall, J. Jaumot, R. Tauler, A. de Juan, A. Gorzsás, Vibrational spectroscopic image analysis of biological material using multivariate curve resolution-alternating least squares (MCR-ALS), Nat. Protoc. 10 (2) (2015) 217–240.
[73] G. Mickisch, S. Fajta, G. Keilhauer, E. Schlick, R. Tschada, P. Alken, Chemosensitivity testing of primary human renal cell carcinoma by a tetrazolium based microculture assay (MTT), Urol. Res. 18 (2) (1990) 131–136.
[74] J. O'Brien, I. Wilson, T. Orton, F. Pognan, Investigation of the Alamar blue (resazurin) fluorescent dye for the assessment of mammalian cell cytotoxicity, Eur. J. Biochem. 267 (17) (2000) 5421–5426.
[75] Methods for dilution antimicrobial susceptibility tests for Bacteria that grow aerobically, in: C.A.L.S.I. CLSI (Ed.), Clinical and Laboratory Standards Institute, Wayne, PA, 2009.